

Satellite Observations and Modelling of Transport in the Upper Troposphere through the Lower Mesosphere During the 2006 Major Stratospheric Sudden Warming

Gloria L. Manney^{1,2}, Robert S. Harwood³, Ian A. MacKenzie³, Ken Minschwaner², Douglas R. Allen⁴, Michelle L. Santee¹, Kaley A. Walker^{5,6}, Michaela I. Hegglin⁵, Alyn Lambert¹, Hugh C. Pumphrey³, Peter F. Bernath^{7,6}, Chris D. Boone⁶, Michael J. Schwartz¹, Nathaniel J. Livesey¹, William H. Daffer¹, and Ryan A. Fuller¹

¹Jet Propulsion Laboratory, California Institute of Technology, Pasadena, CA USA

²New Mexico Institute of Mining and Technology, Socorro, NM USA

³University of Edinburgh, Edinburgh, United Kingdom

⁴Dordt College, Sioux Center, Iowa, USA

⁵University of Toronto, Toronto, Ontario, Canada

⁶University of Waterloo, Waterloo, Ontario, Canada

⁷University of York, Heslington, York, United Kingdom

Abstract. An unusually strong and prolonged stratospheric sudden warming (SSW) in January 2006 was the first major SSW for which globally distributed long-lived trace gas data are available covering the upper troposphere through the lower mesosphere. We use Aura Microwave Limb Sounder (MLS), Atmospheric Chemistry Experiment-Fourier Transform Spectrometer (ACE-FTS) data, the SLIMCAT Chemistry Transport Model (CTM), and assimilated meteorological analyses to provide a comprehensive picture of transport during this event. The upper tropospheric ridge that triggered the SSW was associated with an elevated tropopause and layering in trace gas profiles in conjunction with stratospheric and tropospheric intrusions. Anomalous poleward transport (with corresponding quasi-isentropic troposphere-to-stratosphere exchange at the lowest levels studied) in the region over the ridge extended well into the lower stratosphere. In the middle and upper stratosphere, the breakdown of the polar vortex transport barrier was seen in a signature of rapid, widespread mixing in trace gases, including CO, H₂O, CH₄ and N₂O. The vortex broke down slightly later and more slowly in the lower than in the middle stratosphere. In the middle and lower stratosphere, small remnants with trace gas values characteristic of the pre-SSW vortex lingered through the weak and slow recovery of the vortex. The upper stratospheric vortex quickly reformed, and, as enhanced diabatic descent set in, CO descended into this strong vortex, echoing the fall vortex development. Trace gas evolution in the SLIMCAT CTM agrees well with that in the satellite trace gas data from the upper troposphere through the middle stratosphere. In the upper stratosphere and lower mesosphere, the SLIMCAT simulation does not capture the strong descent of mesospheric CO and H₂O values into the reformed vortex; poor CTM performance in the upper stratosphere and lower mesosphere results primarily from biases in the diabatic descent in assimilated analyses.

1 Introduction

A strong and prolonged Arctic major stratospheric sudden warming (SSW) began in January 2006 (e.g., Hoffmann et al., 2007; Siskind et al., 2007; Manney et al., 2008b). Coy et al. (2008) showed evidence suggesting that this SSW was forced by waves propagating from an upper tropospheric ridge that developed over the North Atlantic after mid-January. Analysis of satellite temperature measurements extending into the mesosphere showed that the stratopause completely broke down during the SSW, then reformed at very high (>75 km) altitude afterward (Siskind et al., 2007; Manney et al., 2008a,b). Not only was the 2006 major SSW one of the strongest and most prolonged on record, and thus of particular interest in its own right, but also, prior to this event, insufficient trace gas data were available to provide

a complete picture of middle atmosphere transport during a major warming.

A few detailed modelling studies of transport during major SSWs have been done (e.g., Manney et al., 2005b; Konopka et al., 2005), focusing on the middle and lower stratosphere, but trace gas data to assess model performance were largely unavailable. Leovy et al. (1985) used Limb Infrared Monitor of the Stratosphere (LIMS) ozone (O₃) data to illuminate some aspects of transport in the middle and lower stratosphere during the February 1979 major SSW, and Manney et al. (1994a) compared LIMS O₃ with mechanistic model simulations to further investigate the origins of the observed features. Randall et al. (2005) reconstructed a “proxy” O₃ field from observations from several solar occultation instruments to compare with the model results of Manney et al. (2005b) during the southern hemisphere (SH) major SSW in September 2002. Lahoz et al. (1994), Manney et al. (1994c), and Sutton et al. (1994) showed some aspects of stratospheric transport during minor SSWs using Upper Atmosphere Research Satellite (UARS) Microwave Limb Sounder (MLS), Cryogenic Limb Array Etalon Spectrometer (CLAES), and Improved Stratospheric And Mesospheric Sounder (ISAMS) long-lived trace gas data (including nitrous oxide, N₂O, and water vapour, H₂O). Allen et al. (1999) showed observed patterns of transport in ISAMS carbon monoxide (CO) during a minor SSW in January 1992, including descent of mesospheric CO into the stratospheric vortex.

These observational studies have been limited by several factors: There were no major SSWs when UARS MLS, CLAES, or ISAMS (instruments with hemispheric daily coverage) were operating, and although the UARS Halogen Occultation Experiment (HALOE) solar occultation instrument continued to provide data until late 2005, it had very poor high latitude coverage during winter. Thus no extensive measurements of long-lived tracers (e.g., N₂O, methane (CH₄), H₂O, CO) have been available during previous major SSWs. Transport studies using O₃ are limited to the middle and lower stratosphere, where dynamical timescales are close to or shorter than its chemical lifetime. Even in these regions, however, chemical effects can play a substantial role in O₃ evolution (e.g., heterogeneous chemistry in the lower stratosphere (e.g., WMO, 2007); formation of “low-ozone pockets” in the middle stratosphere (e.g., Manney et al., 1995)).

Even more critically, data to provide a complete picture of transport in the upper troposphere through the lower mesosphere, have been unavailable until recently. CO (a good tracer of upper stratosphere/lower mesosphere (USLM) transport) was available from ISAMS for only a portion of one northern hemisphere (NH) and one SH winter. O₃ (which becomes a good tracer in the upper troposphere/lower stratosphere, UTLS) from LIMS and UARS MLS and CLAES did not extend into the lowermost stratosphere (lower limits were ~100 hPa). Similarly, measurements of CH₄ and N₂O from CLAES were limited to the stratosphere. Even more critically, it has recently become

apparent that the atmosphere is closely coupled from the upper troposphere through the mesosphere (e.g., Shepherd, 2007, 2008). This is particularly evident during major SSWs as planetary-scale waves propagating from the upper troposphere into the polar upper stratosphere drive the breakdown of the stratospheric vortex, and result in changes in gravity-wave propagation and breaking, leading to cooling of the mesosphere (related to anomalous gravity wave filtering) and enhanced radiative cooling near the stratopause (Hoffmann et al., 2007; Siskind et al., 2007; Coy et al., 2008; Manney et al., 2008b, and references therein). Full understanding of how these dynamical and radiative changes affect transport requires the study of trace gas distributions over the entire altitude range from the upper troposphere to the mesosphere; such comprehensive datasets are only now becoming available from recent satellite measurements.

With the launch of NASA's Earth Observing System (EOS) Aura satellite in July 2004, carrying an advanced MLS instrument (Waters et al., 2006), we now have near-global daily measurements of several long-lived tracers of transport. Detailed information on transport from the lower stratosphere through the lower mesosphere is provided by MLS H_2O , N_2O and CO , and in the UTLS by MLS O_3 , HNO_3 , H_2O and CO . In addition to MLS, the Atmospheric Chemistry Experiment–Fourier Transform Spectrometer (ACE-FTS) solar occultation instrument (Bernath et al., 2005), which has been taking data since early 2004, measures a large suite of species including long-lived tracers such as CH_4 that are not measured by MLS. While ACE-FTS provides observations at no more than 15 longitudes around a single latitude in each hemisphere per day, its orbit is designed to provide good coverage of polar regions in winter, thus much information on transport can be extracted from these sparse data by mapping in vortex-centered coordinates (e.g., Manney et al., 1999b, 2007).

Manney et al. (2008b) described the synoptic evolution in the middle stratosphere through the lower mesosphere during the 2006 SSW. The conditions for a major warming (zonal mean zonal wind and temperature gradient reversal north of 60°N at 10 hPa) were fulfilled on 21 January, with a preceding strong minor warming starting around 8 January. Upper stratospheric winds reversed around 9 January and remained easterly in the polar regions until early February, after which a very strong westerly jet reformed around 45°N and moved poleward. Though a very strong upper stratospheric vortex reformed quickly after the warming, the middle stratospheric vortex recovered very slowly, and the lower stratospheric vortex remained weak and ill-defined for the remainder of the winter. As is common after early (December or January) major SSWs (Manney et al., 2005a, and references therein), the final warming was slow and late, with 10 hPa zonal mean winds not reversing permanently until early May. Initial examinations of Arctic trace gas data from MLS and ACE-FTS (Manney et al., 2008a; Jin et al., 2008), reports of anomalous stratospheric effects of energetic particle precipitation in

2006 after the SSW (Randall et al., 2006), and a low column O_3 event associated with the upper tropospheric ridge forcing the 2006 SSW (Keil et al., 2007) all point to highly anomalous transport throughout the upper troposphere, stratosphere and mesosphere during the 2006 Arctic winter.

Here we use Aura MLS and ACE-FTS data, along with diagnostics calculated from assimilated meteorological analyses, to detail large-scale transport in the entire region covering the upper troposphere through the lower mesosphere during the 2005–2006 NH winter, focusing on the SSW. Observed transport is compared with simulations using the SLIMCAT Chemistry Transport Model (CTM) (Chipperfield, 2006) and, in the UTLS, with high-resolution Lagrangian calculations. Section 2 provides a description of the datasets and models used. In Section 3, we provide an overview of transport in the middle and lower stratosphere in the context of the vortex evolution described above, and relate these results to those from previous studies. We then turn to examination of the regions that have not been studied in any detail before: Data were not available for comprehensive studies of the USLM until recently; Section 4) provides a detailed description of observed and modeled transport in this region. Section 5 gives a view of modeled and observed transport in the UTLS made possible by recent satellite data extending to these levels, focusing on the dynamical processes forcing the SSW. A summary and conclusions are given in Section 6.

2 Data, Analysis, and Models

2.1 Meteorological Data and Analysis

The primary meteorological dataset used here is the Goddard Earth Observing System Version 5.10 (GEOS-5) analysis from NASA's Global Modelling and Assimilation Office (GMAO), described by Reinecker et al. (2008). GEOS-5 uses the Gridpoint Statistical Analysis method of Wu et al. (2002), a 3D-Variational system, and a six-hour analysis window. The interface between the observations and the general circulation model (GCM) is performed using the incremental analysis update (IAU) approach (Bloom et al., 1996), which avoids shocking the model, thus producing smoother analyses. GEOS-5 analyses are provided on 72 model levels from the surface to 0.01 hPa (~ 75 km), on a 0.5° latitude by 0.6667° longitude grid.

European Centre for Medium-Range Weather Forecasts (ECMWF) analyses are used to drive the SLIMCAT CTM. ECMWF analyses are from a 4D-Var system based on a spectral general circulation model (e.g., Simmons et al., 2005). Beginning in February 2006, ECMWF fields are from a T799 ($\sim 0.3^\circ$ horizontal resolution)/91-level system with a model top at 80 km (e.g., Untch et al., 2006, and other ECMWF newsletters, available at <http://www.ecmwf.int/publications/newsletters/>); before that

date, the operational data are from a T512/60-level model with a top at 60 km.

Manney et al. (2008b) provide further details of the GEOS-5 and ECMWF analyses; detailed comparisons of temperatures with satellite data (including MLS) show large, but differing biases in the ECMWF and GEOS-5 analyses during and following the 2006 SSW.

Derived meteorological products (DMPs) for ACE and MLS have been calculated from the GEOS-5 analyses, as described in detail by Manney et al. (2007). These products comprise meteorological variables (winds, temperature, potential vorticity (PV)) and fields calculated from them (e.g., equivalent latitude (EqL) and tropopause heights) interpolated to the observation locations and times of the satellite instruments. The DMPs are calculated operationally for both instruments and MLS DMPs are publicly available (Manney et al., 2007). We use the GEOS-5 DMPs for ACE and MLS to map the data into EqL/potential temperature (θ) coordinates and to provide information on the location of measurements with respect to the vortex for vortex averages; details of EqL mapping and vortex averaging using the DMPs are as described by Manney et al. (2007).

The evolution of the trace gas fields is compared with effective diffusivity (K_{eff}), calculated as described by Allen and Nakamura (2001). K_{eff} , which is expressed here as log-normalized equivalent length, provides a measure of mixing and transport barriers (e.g., Haynes and Shuckburgh, 2000a,b; Allen and Nakamura, 2001; Tan et al., 2004), with low values representing transport barriers and high values representing strong mixing. The K_{eff} calculations for this period are taken from a long-term run of the advection-diffusion model of Allen and Nakamura (2001) that was driven with Met Office analyses (Swinbank and O'Neill, 1994; Swinbank et al., 2002, 2004) until 13 March 2006 (the time of a major change in the Met Office assimilation system) and with GEOS-4 analyses after that date. The Met Office analyses come from a system with a lower model top (~ 60 km) than the GEOS and ECMWF analyses, and are thus expected to be less reliable in the upper stratosphere.

2.2 Microwave Limb Sounder Data

MLS measures millimeter- and submillimeter-wavelength thermal emission from the limb of Earth's atmosphere. Detailed information on the measurement technique and the MLS instrument on the EOS Aura satellite is given by Waters et al. (2006). Aura is in a 98° inclination orbit, and the Aura MLS fields-of-view point in the direction of orbital motion and vertically scan the limb in the orbit plane, leading to data coverage from 82°S to 82°N latitude on every orbit. Vertical profiles are measured every 165 km along the sub-orbital track and have a horizontal resolution of ~ 200 – 300 km along-track and ~ 3 – 9 km across-track. Vertical resolution of the Aura MLS data is typically ~ 3 – 4 km in the upper troposphere through the middle stratosphere, degrading to 5–8 km

in the upper stratosphere and mesosphere, depending on the product (Livesey et al., 2007).

We use version 2.2 (v2.2) H_2O , N_2O , CO , HNO_3 , and O_3 from MLS to detail transport processes from the upper troposphere into the lower mesosphere, and MLS temperatures for radiation calculations. Validation of N_2O and H_2O is discussed by Lambert et al. (2007), of CO by Pumphrey et al. (2007) and Livesey et al. (2008), of O_3 by Froidevaux et al. (2008) and Livesey et al. (2008), of HNO_3 by Santee et al. (2007), and of temperature by Schwartz et al. (2008). For maps, MLS data are gridded using weighted averages of each day's data in the region around each gridpoint.

2.3 Atmospheric Chemistry Experiment Data

SCISAT-1, otherwise known as ACE (Bernath et al., 2005), was launched in August 2003. The primary instrument is the ACE-FTS, a Fourier transform spectrometer featuring high resolution (0.02 cm^{-1} , corresponding to a $\pm 25\text{ cm}$ maximum optical path difference) and broad spectral coverage in the infrared (750 – 4400 cm^{-1}). ACE-FTS works primarily in the solar occultation mode, collecting atmospheric limb measurements using the sun as a radiation source. Version 2.2 of the ACE-FTS retrievals (Boone et al., 2005) is used here, except for O_3 , for which the ACE-FTS product known as “version 2.2 ozone update” is used (Dupuy et al., 2008). Validation of ACE data is described in a special issue of *Atmospheric Chemistry and Physics*. In addition to other species, ACE-FTS N_2O (Strong et al., 2008), H_2O (Carleer et al., 2008), CO (Clerbaux et al., 2008) and CH_4 (De Maziere et al., 2008) have been shown to be useful throughout the stratosphere, and ACE-FTS CO , O_3 and H_2O down into the upper troposphere (Hegglin et al., 2008). ACE-FTS vertical resolution is ~ 3 – 4 km. Latitudes of measurements vary over an annual cycle with coverage as high as $\pm 85^\circ$ and an emphasis on the polar regions in winter and spring.

2.4 Models and Calculations

SLIMCAT 3D CTM (Chipperfield et al., 1996; Chipperfield, 1999) simulations are compared with ACE-FTS and MLS observations. Feng et al. (2005) show that the updated SLIMCAT model, with a hybrid σ – θ vertical coordinate and a more sophisticated radiation scheme, produces more realistic representations of tracer transport than the previous scheme, which tended to underestimate descent. The simulation analyzed here has $2.8^\circ \times 2.8^\circ$ horizontal resolution, with 50 levels from the surface to 3000 K (~ 60 km), using purely isentropic surfaces above 350 K. For each MLS measurement an equivalent sample, interpolated to the same location, is taken from the model at the nearest available time (always within 15 minutes). Winds and temperatures sampled at T42 resolution from the operational ECMWF analyses (e.g., Simmons et al., 2005) are used to drive the SLIMCAT model. Because ECMWF switched from the T512, 60-level model

to the T799, 91-level model with top at 0.01 hPa on 1 February 2006, the simulations during the first approximately 2/3 of the period shown here are driven with winds and temperatures from a model with a top near 60 km, at some times and places lower than the model top at 3000 K.

The SLIMCAT model run used in this paper (referred to here as “run B”) is based on a previous run (“run A”) with the same basic model configuration that has been continuously simulating the atmosphere since the Aura launch. Run B was initialised for 0 UT on 15 November 2005 using the fields for that time from run A with the exception of O₃, H₂O, HCl, HNO₃ and CO. O₃, H₂O and HCl were replaced by values taken from the v2.2 MLS data for the 24 hours centered on the initialization time by treating the atmosphere as static for that period, gridding the data onto a regular latitude-longitude grid at MLS pressure levels, then interpolating to the model grid. The initial ClONO₂ and reactive chlorine abundances were adjusted so that the total inorganic chlorine remained as in run A. Initial HNO₃ in run B was based on MLS data below 1050K; at higher levels the values from run A were retained. N₂O was treated similarly, except that the transition level was 1450K. MLS CO data were also used in the model initialisation, but because of some vertical oscillations (albeit much less severe in v2.2 than in v1.5 Pumphrey et al., 2007), these data were smoothed in the vertical and then zonally averaged equatorward of 45° and in EqL poleward of 45°. More details of the model configuration are given by Santee et al. (2008).

Results from the Global Modeling Initiative (GMI) “Aura4” run (Strahan et al., 2007, and references therein) were examined to help evaluate differences in transport calculations related to the assimilated meteorological fields used to drive them. The GMI Aura4 run was driven with GEOS-4 (Bloom et al., 2005) fields.

Reverse trajectory (RT) calculations (e.g., Sutton et al., 1994; Manney et al., 1998) are used to examine transport in the UTLS. These calculations are done on isentropic surfaces using GEOS-5 horizontal winds, and are initialized with MLS data eight days prior to the date of interest. They provide an estimate of the fine-scale structure predicted based on transport of the coarse-resolution MLS fields.

Radiation calculations have been done to assess vertical motion for interpretation of the MLS measurements. A longwave band model adapted from the Community Climate Model, Version 2 (CCM2) radiation code (Briegleb, 1992a) is used (the SLIMCAT model also uses a version of this code). This is a 100 cm⁻¹ band model that considers infrared opacity by H₂O, CO₂, O₃, CH₄, N₂O, CFC-11, and CFC-12. The shortwave radiative heating is calculated using the δ -Eddington approximation with 18 spectral bands (Briegleb, 1992b). The CCM2 radiation code has been validated against line-by-line longwave calculations and in comparisons with Earth Radiation Budget Experiment long-wave fluxes and shortwave albedos (Briegleb, 1992a,b). H₂O and O₃ derived from MLS profiles are used for all calculations;

other trace gases, tropospheric temperatures, and tropospheric clouds are based on a combined UARS climatology appropriate for high-latitude winter (Minschwaner et al., 1998). To focus on the sensitivity of diabatic heating to temperature differences, all other inputs are fixed for a given day, and diabatic heating rates (averaged over a day) are calculated from time series of zonal mean profiles of 12-UT temperature from MLS (daily average centered around 12 UT), GEOS-4, GEOS-5 and ECMWF. Manney et al. (2008b) used similar calculations to show that GEOS-5 and ECMWF both misrepresented the diabatic cooling in the USLM on selected days after the SSW, which may be expected to lead to biases in transport model simulations driven with fields from these analyses.

3 SSW and Transport Overview: The Middle and Lower Stratosphere

Examination of MLS, ACE-FTS, and SLIMCAT-modelled trace-gas evolution in the middle and lower stratosphere allows us to verify the general features of transport that are expected from previous model studies and observations during minor SSWs, and to extend those results to provide a detailed description of transport and our ability to model it in this region. Figure 1 shows maps of MLS long-lived tracers in the middle (850 K, ~10 hPa, H₂O) and lower (520 K, ~50 hPa, N₂O) stratosphere, with overlaid GEOS-5 scaled PV (sPV) (e.g., Manney et al., 1994b) contours demarking the strong gradients in the vortex edge region. Other trace gases measured by MLS show a consistent picture at each level. The MLS species’ gradients are closely correlated with the overlaid sPV fields, indicating a consistent representation of the vortex in both the MLS data and the GEOS-5 sPV.

In early winter, the high values of MLS H₂O in the middle stratosphere indicate confined descent within the vortex before the SSW (10 January). A strong Aleutian anticyclone formed during a strong minor warming preceding the major SSW, and was apparent at 10 hPa over the dateline on 10 January. The low H₂O values surrounding the core of the anticyclone (along with low sPV), and elevated values within its core, suggest that low latitude air was drawn up between the anticyclone and vortex and subsequently coiled up inside the anticyclone, as is common during SSWs (e.g. O’Neill et al., 1994) (this picture has been confirmed using RT calculations, not shown). According to Coy et al. (2008), the major SSW was generated on about January 20 at 60°N by an anticyclonic circulation consisting of normally tropical values of PV (see their Figure 1). As seen in our Figure 1, this anticyclonic circulation transports very low H₂O values towards higher latitudes. By 22 January, when zonal mean winds had reversed, the vortex had shrunk into a crescent shape and shifted off the pole, with the anticyclone moving near the pole and containing very low H₂O values indicative of air drawn up from low latitudes (a few days later, by

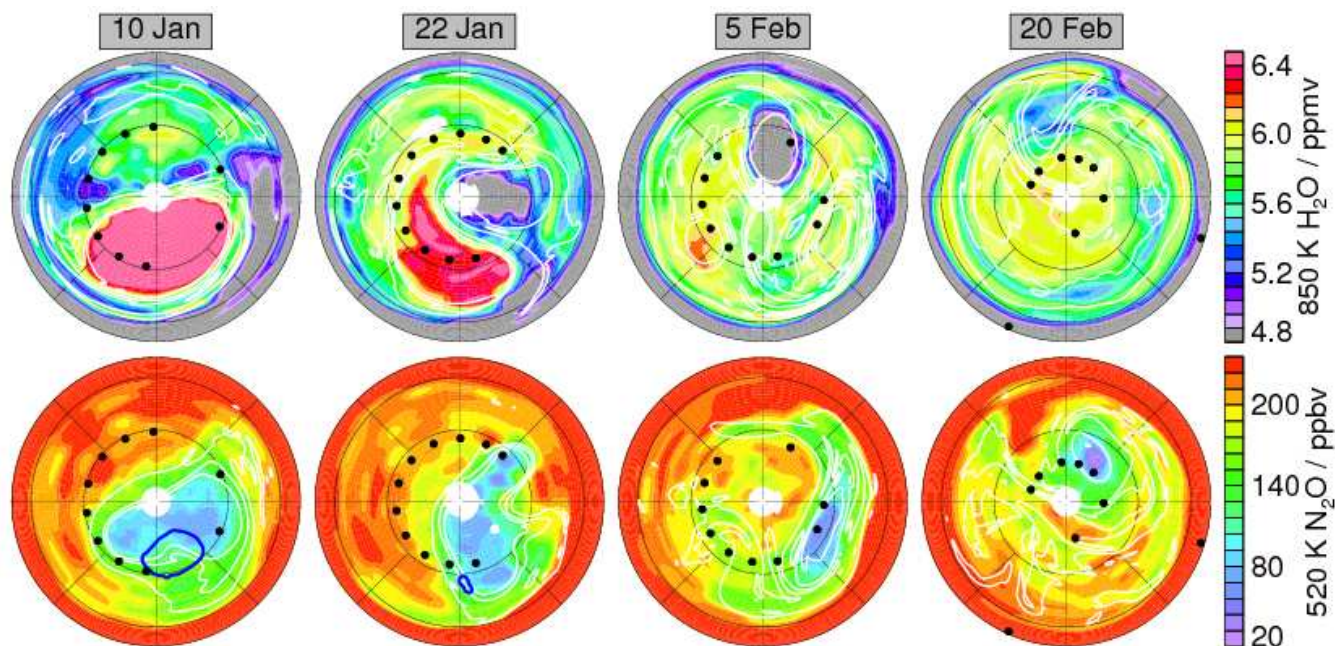


Fig. 1. Maps of MLS long-lived trace gases in the middle (850 K, ~ 10 hPa, ~ 30 km) and lower (520 K, ~ 50 hPa, ~ 19 km) stratosphere before (10 January), during (22 January, 5 February) and after (20 February) the 2006 SSW. H_2O is shown at 850 K and N_2O at 520 K. Overlaid white contours are sPV in the vicinity of the vortex edge; overlaid blue contour at 520 K is a temperature of 195 K, near the PSC formation threshold (only present on 10 and 22 January). Black dots show ACE measurement locations on each day. Projection is orthographic, with 0° longitude at the bottom and 90°E to the right; domain is 0 to 90°N .

27 January, the anticyclone was centered over the pole (not shown). Decreasing H_2O in the vortex and increasing values spreading through mid-latitudes indicate the strong mixing during the SSW. The vortex continued to decay, so that by 5 February, only a small remnant of high H_2O remained near 300°E , with a small, but strong, anticyclone (low H_2O) centered near the date line. By 20 February, H_2O gradients were very weak throughout the hemisphere, suggesting complete breakdown of the transport barriers that inhibit mixing. The vortex and tracer gradients remained weak through the rest of the winter.

The lower stratosphere was affected by the SSW somewhat later than higher altitudes. On 10 January, the vortex was relatively large and strong, and shifted towards the Greenwich meridian, with a large region of temperatures below the PSC formation threshold (blue overlay) on the equatorward edge, in a typical lower stratospheric wintertime pattern. Low levels of N_2O in the vortex are a signature of descent. By 22 January, the vortex was quite distorted, and beginning to shrink, but relatively strong sPV gradients remained along the vortex edge and N_2O values remained low within the vortex; only a very small region of PSC temperatures persisted right at the vortex edge. By 5 February, the vortex had shrunk to a narrow crescent near 60°N , with low N_2O values limited to a small region in its interior.

By 20 February, only a small vortex remnant persisted near 120°E . This well-defined remnant, with very low N_2O values, lingered throughout the winter, eventually being encompassed by a larger, but weak, reformed vortex with intermediate N_2O values (not shown).

The 22 January and 5 February fields show the vortex and MLS trace gas signatures (high H_2O , low N_2O) tilting strongly westward with height from the lower to the middle stratosphere. Similar vortex behavior has been reported in previous studies of SSWs (e.g., Fairlie et al., 1990; Manney et al., 1994a, 1999a, 2005b), and is evidence of upward propagation of wave activity according to linear theory.

Figures 2 and 3 show EqL/time plots of observed and SLIMCAT-modelled trace gases at 850 and 520 K, respectively. K_{eff} is also shown to identify regions of mixing and transport barriers. We show MLS N_2O and CO , and ACE-FTS CH_4 at 850 K. For MLS and SLIMCAT (which was sampled at MLS observation locations), each EqL/time bin is filled with a number of points comparable to what would result from a zonal mean, typically 10 to 50 points in each EqL bin; in contrast, the sparse ACE sampling results in a typical bin being represented by one to a few data points. Thus, the ACE fields are not only less complete, but noisier and more dependent on the details of the sampling (e.g., Manney et al., 2007). Subject to this constraint, ACE-FTS N_2O and CO

(not shown) agree well with those from MLS, and H₂O from both instruments evolves consistently with the fields shown here. CH₄, like N₂O, decreases with altitude, and thus low values in the vortex are the signature of confined descent. The K_{eff} evolution indicates that the transport barrier almost completely breaks down at 850 K at the beginning of February, and remains weak and encloses a small area throughout February; sPV gradients strengthen in early March, and although they remain much weaker than before the SSW, the K_{eff} suggests re-establishment of a weak transport barrier near 50°EqL. Consistent with the evolution of K_{eff} and sPV, N₂O and CH₄ show strong gradients across the vortex edge before the warming, with low N₂O and CH₄ spreading out through mid-EqLs during the warming and forming weak, but significant, gradients parallel to those in K_{eff} during the weak recovery. High CO descending in the vortex did not reach down to 850 K until early January (see below). During the vortex breakdown, mixing is readily apparent in the high MLS CO values spreading out to ~40°EqL. A small remnant of vortex air at highest EqLs can be identified throughout the SSW, with more moderate N₂O and CH₄ values at mid-EqLs forming slightly stronger gradients as a transport barrier reforms in late February.

SLIMCAT appears to do a very good job of reproducing the quasi-horizontal transport and mixing associated with the SSW in the middle stratosphere, with only small differences in detail in the time evolution: Slightly lower N₂O and CH₄ in early February, and slightly stronger N₂O and CH₄ gradients as the vortex weakly reforms, suggest the possibility of an underestimate in mixing in SLIMCAT. SLIMCAT vortex CO values, higher than MLS in December, and lower in January, suggest inaccuracies in the diabatic descent (calculated from ECMWF temperatures) used in the model. Since SLIMCAT had apparently not brought down enough CO to this level before the warming to closely match MLS (and ACE-FTS, which agrees well with MLS, not shown), a meaningful assessment of agreement during and after the SSW cannot be made; SLIMCAT does, however, show a sudden increase in values at mid-EqLs at the end of January, with timing and qualitative pattern similar to that observed.

At 520 K in the lower stratosphere (Figure 3), we show MLS N₂O and O₃. Here, the vortex was relatively strong and cold until late January. The decrease seen in O₃ in the vortex core during January has been shown to be inconsistent with transport (note that N₂O decreases at this time and place, indicating diabatic descent that would increase O₃) and consistent with chemical loss; rough estimates using MLS data suggest about 0.5–0.7 ppmv chemical loss during January 2006 (Braathen et al., 2006). The vortex breakdown during the SSW began at the end of January, and was more gradual and less complete than that at higher levels, with a region of reduced mixing (seen as lingering low K_{eff} values) remaining in the vortex core throughout the winter. This is consistent with the clearly identifiable remnants of vortex (low N₂O) air seen in Figure 1. The observed evolution of H₂O (MLS

and ACE-FTS) and CH₄ (ACE-FTS), not shown, is consistent with that of N₂O.

SLIMCAT shows slightly lower 520 K N₂O (and higher H₂O, not shown) inside the vortex and its remnants throughout the period shown, suggesting the possibility that lower stratospheric descent in SLIMCAT may be slightly too strong. In early February in the region outside the vortex remnant, air with low N₂O values spreads to lower EqLs in SLIMCAT than in MLS, suggesting more mixing into mid-latitudes from the outer part of the vortex. Since stronger mixing would tend to *increase* vortex N₂O, the presence of lower values in SLIMCAT than in MLS reinforces the evidence that descent in the vortex in SLIMCAT is too strong.

The decrease in SLIMCAT O₃ in January to early February is very similar in magnitude and evolution to that in MLS. This is consistent with the results of Santee et al. (2008), who show, however, that the good agreement in polar O₃ evolution may result from a fortuitous combination of conditions, since SLIMCAT chlorine activation and partitioning show significant deficiencies in the model formulation used here.

EqL/θ snapshots of MLS N₂O (Figure 4) summarize the 3D transport in the middle and lower stratosphere during the SSW. On 10 January, the vortex was still strong throughout the stratosphere, and N₂O shows the signature of vortex descent, with very similar fields in SLIMCAT and MLS; slightly looser packing in the vertical of contours in the vortex in SLIMCAT above ~600 K and slightly tighter below is consistent with the previous suggestion of stronger descent at the lowest levels in SLIMCAT. By 21 January, the vortex has broken down in the upper stratosphere, reflected in higher N₂O values encroaching towards the polar regions at the highest levels shown; slightly lower mid-EqL N₂O values in SLIMCAT above ~800 K suggest stronger descent in this region. N₂O shows the signature of continued vortex descent in the lower stratosphere. By 5 February, the vortex comprises only a small remnant in the middle to lower stratosphere, and the low N₂O confined in that remnant has continued to descend. This vortex remnant is still present in the middle stratosphere through ~20 February, and in the lower stratosphere as late as 15 March (not shown).

Away from the polar vortex, SLIMCAT appears to do a fairly good job of maintaining the subtropical transport barrier in the middle to upper stratosphere, as seen in strong horizontal N₂O gradients, comparable to those in MLS, near 20°EqL above ~30 km. This is consistent with the results of Feng et al. (2005) and Santee et al. (2008) showing a better representation of transport in this version of the SLIMCAT model.

The overview given above provides observational confirmation of aspects of stratospheric transport during strong SSWs previously documented in modelling studies, and details other aspects that are consistent with expectations from dynamical studies. General features are common to most major SSWs: The vortex and trace gases confined within it tilt

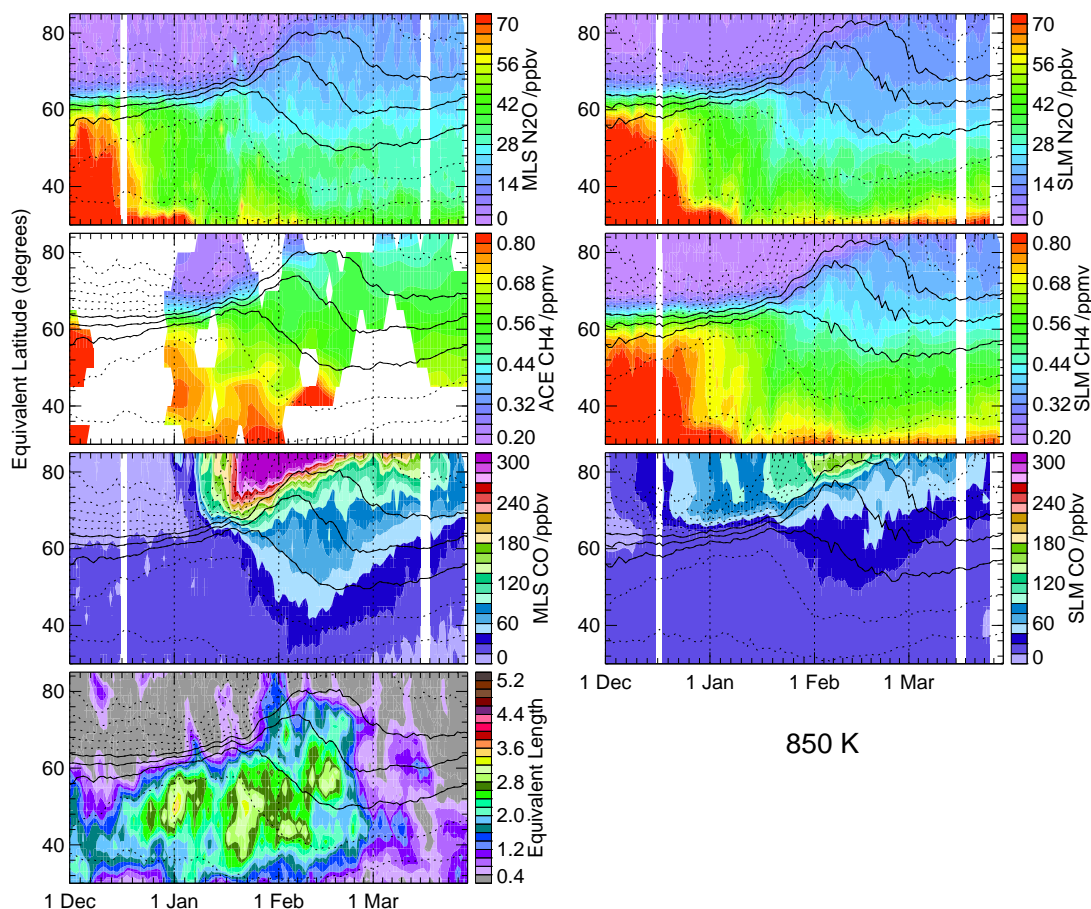


Fig. 2. Equivalent latitude (EqL)-Time plots of observed (left) and SLIMCAT modelled (right) N_2O (MLS, top), CH_4 (ACE-FTS, center) and CO (MLS, bottom) during the 2005-2006 NH winter on the 850 K isentropic surface. Lower left panel is effective diffusivity (K_{eff}) expressed as log-normalized equivalent length. Overlays are GEOS-5 (ECMWF) sPV contours on MLS and ACE-FTS (SLIMCAT) plots, with solid contours at values that are typically in the region of strong gradients demarking the vortex edge.

westward with height. Material is drawn up around the vortex and coils up in the high-latitude anticyclone that forms as the vortex breaks down; tongues of material are also drawn off vortex. The transport barrier breaks down earlier and more completely in the middle than in the lower stratosphere, consistent with the dynamical evolution of the vortex shown in previous studies (e.g., Fairlie et al., 1990; Manney et al., 2005a). Features that are specific to the 2006 SSW include the complete disappearance of a vortex transport barrier and dispersal of vortex air resulting from the unusual strength of this SSW, and the slow and weak reformation of the vortex transport barrier and re-establishment of horizontal trace gas gradients reflect the prolonged nature of the 2006 SSW.

Figure 5 shows the evolution of vortex-averaged trace gases in the lower stratosphere through the lower mesosphere, placing the middle and lower stratospheric evolution discussed above in the context of transport in the en-

tire middle atmosphere. For CH_4 , the analyzed SLIMCAT fields have been sampled near the ACE measurement locations, and the apparent increase prior to the observing gap in late December is a result of the change in latitude of ACE sampling at that time, as described by Manney et al. (2007). Because SLIMCAT was initialized with CH_4 that was inconsistent with that from ACE-FTS, it is appropriate to compare gradients and time evolution, but not quantitative values. The evolution of N_2O , CH_4 , and CO in the lower through the middle stratosphere is consistent with the transport detailed above, showing abrupt increases in N_2O and CH_4 and decreases in CO in late January coincident with the vortex breakdown in the middle to lower stratosphere. SLIMCAT shows slightly smaller increases when the vortex breaks down (suggesting less mixing in the middle stratosphere), and a generally slightly stronger downward tilt of the contours indicating more descent; but these differences

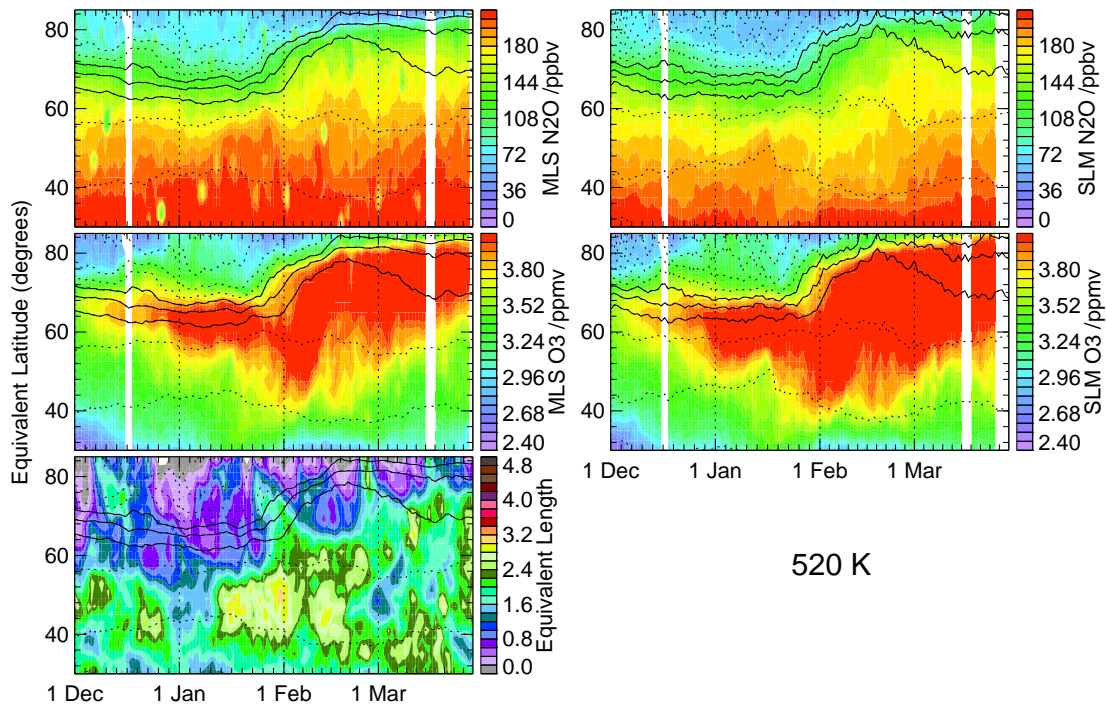


Fig. 3. As in Figure 2, but showing MLS and SLIMCAT N_2O and O_3 at 520 K.

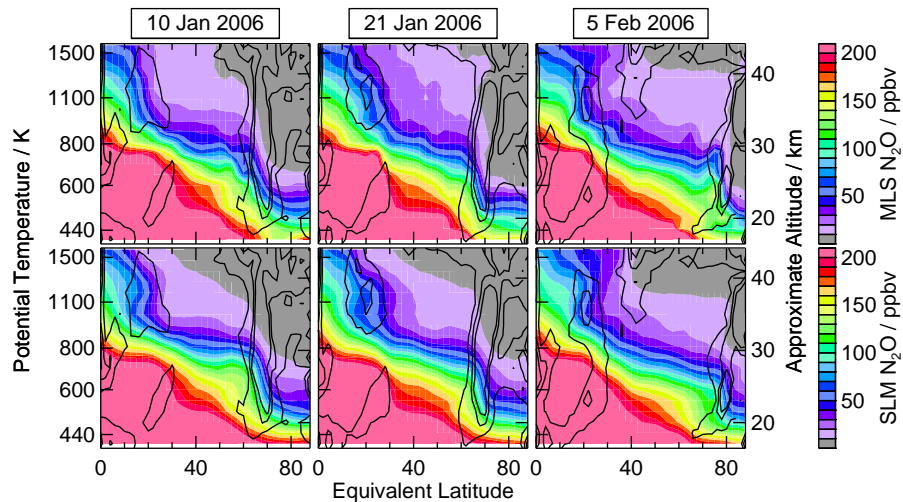


Fig. 4. EqL/ θ plots of MLS and SLIMCAT N_2O before, during and after the 2006 SSW. Vertical range is 400 to 1600 K. Overlays are PV gradients from GEOS-5, normalized to the hemispheric average values at each θ level.

are very small. Before the warming, the SLIMCAT simulations suggest slower descent than the satellite data in the middle stratosphere and above, but stronger descent below 600 K for the same period. While SLIMCAT CH_4 values above ~ 700 K are initially lower than those for MLS, they do not decrease as rapidly as in the ACE-FTS observations,

and SLIMCAT CO values below ~ 1700 K do not increase as rapidly as those in MLS. Stronger descent in SLIMCAT than in MLS in the lower stratosphere in a similar simulation was previously noted by Santee et al. (2008). After the SSW, vortex averaged N_2O and CH_4 in the middle and lower stratosphere remained nearly constant, consistent with the weak

recovery at these levels noted above (the apparent increase in CH_4 in late March reflects the changing sampling of ACE-FTS). The behavior of CO in the USLM is discussed further in Section 4.

The results shown above confirm and extend those of previous studies that examined some aspects of transport during SSWs. Very few previous studies have discussed vortex evolution or, especially, transport at higher levels, so our understanding of transport during SSWs in the upper stratosphere and mesosphere has been very rudimentary. In the following section, we detail that evolution using MLS data and the SLIMCAT simulation.

4 The Upper Stratosphere and Lower Mesosphere

4.1 Observed and SLIMCAT-Modelled Transport

Figure 6 shows the synoptic evolution of the vortex and MLS CO during the period in maps at 1700 K (~ 1.5 hPa, upper stratosphere), 2500 K (~ 0.3 hPa, near stratopause), and 3200 K (~ 0.1 hPa, mesosphere). As is typical for early winter (e.g., Allen et al., 1999, 2000), by January high levels of CO had been transported downward from the mesosphere into the upper stratospheric vortex. On 10 January, the USLM vortex was already highly distorted and shifted off the pole, resulting in the zonal mean easterlies previously reported at this time and level (Manney et al., 2008b). The vortex and CO structure suggest substantial mixing of tongues of air with high CO pulled off the distorted and decaying vortex into midlatitudes. The anticyclone (low CO at high latitudes) was already over the pole at these levels, and remained so through 22 January. By 5 February, when USLM winds had begun to recover (Manney et al., 2008b), a large, pole-centered vortex had reformed, and CO was increasing throughout the vortex at 3200 K and in the vortex core at 2500 and 1700 K. By 20 February, high CO (comparable to values well before the SSW, not shown) filled the lower mesospheric vortex (3200 and 2500 K), and maximum values in the upper stratospheric (1700 K) vortex core were comparable to those before the SSW. The vortex began to weaken at these levels by 15 March, more so at the highest levels, and CO showed a corresponding large decrease at 3200 K and slight decrease at 2500 K (not shown).

Vortex-averaged CO (Figure 5), as well as CH_4 , shows the patterns of vortex descent in the upper stratosphere and into the mesosphere. Figure 7 shows the time evolution of CO and K_{eff} as a function of EqL in the upper stratosphere at 1700 K; ACE-FTS CO (not shown) shows similar values and time evolution to those seen in MLS CO. The evolution of K_{eff} indicates a complete breakdown of the vortex transport barrier, with high values indicative of strong mixing extending near the pole after mid-January. A strong transport barrier reforms almost immediately north of 40°N , along with reformation of a strong vortex. As expected from general studies of descent

in the vortex (e.g., Fisher et al., 1993; Allen et al., 1999), the signature of strong, relatively monotonic descent is seen before the SSW, until early January. Because CO values are at very low stratospheric background values (~ 12 – 15 ppbv, e.g., Flocke et al., 1999) outside the vortex (Figure 7), and very high values have been transported down into the vortex through the middle stratosphere when the SSW starts, the signature of the vortex breakdown is very dramatic in the vortex averages: In early January, CO values begin to dramatically decrease, most rapidly at levels above ~ 1700 K, with high values lingering until late January in the middle stratosphere. As seen in Figure 7, this signature results primarily from the mixing of high values from the relatively small area of the vortex into the larger midlatitude area as the vortex breaks down; very low values extend near the pole at this time. After the SSW, starting in early February when the USLM vortex is reforming and becoming very strong (e.g., Manney et al., 2008b, also see Figure 6 and overlaid sPV contours in Figure 7), high MLS CO again descends from the mesosphere, echoing the descent seen in fall/early winter; at 1700 K, the signature of this is an increase in CO in the vortex core starting in early February, and spreading throughout the vortex by the end of March. A similar signature is seen in ACE-FTS vortex-averaged CH_4 (until early March, when sampling effects become significant), and the enhanced vortex descent after the warming is consistent with results shown by Randall et al. (2006), Manney et al. (2008a) and Jin et al. (2008).

In the USLM, the SLIMCAT fields show significant discrepancies compared to the satellite observations: Before the SSW, the high vortex CO did not descend as far, suggesting that diabatic descent in the model was too weak at these levels. While the signature of vortex breakdown during the major SSW is generally captured well, the abrupt decrease in CO is slightly later above ~ 1700 K, and elevated values linger into February at the highest levels shown; Figure 7 shows slightly higher SLIMCAT than MLS CO near the pole in late January. These patterns suggest some deficiencies in mixing in the model. The largest discrepancy, however, is the failure of the model to produce high CO descending into the vortex immediately after the warming; the signature of this descent does not begin until March (with high vortex CO descending to 1700 K only at the end of March), and then appears to be too rapid (Figure 5). This points to significant biases in the diabatic descent in SLIMCAT during the recovery from the SSW. The ECMWF sPV contours overlaid on the SLIMCAT plots in Figure 7 show substantial differences from those from GEOS-5 on the MLS plots, with a weaker/late vortex reformation after the SSW. These differences are consistent with those noted by Manney et al. (2008b), and related to the biases in the analyzed temperatures and winds from both GEOS-5 and ECMWF; these temperature biases are expected to strongly influence calculated diabatic descent rates.

Figure 8 shows MLS, ACE-FTS, and SLIMCAT H_2O and

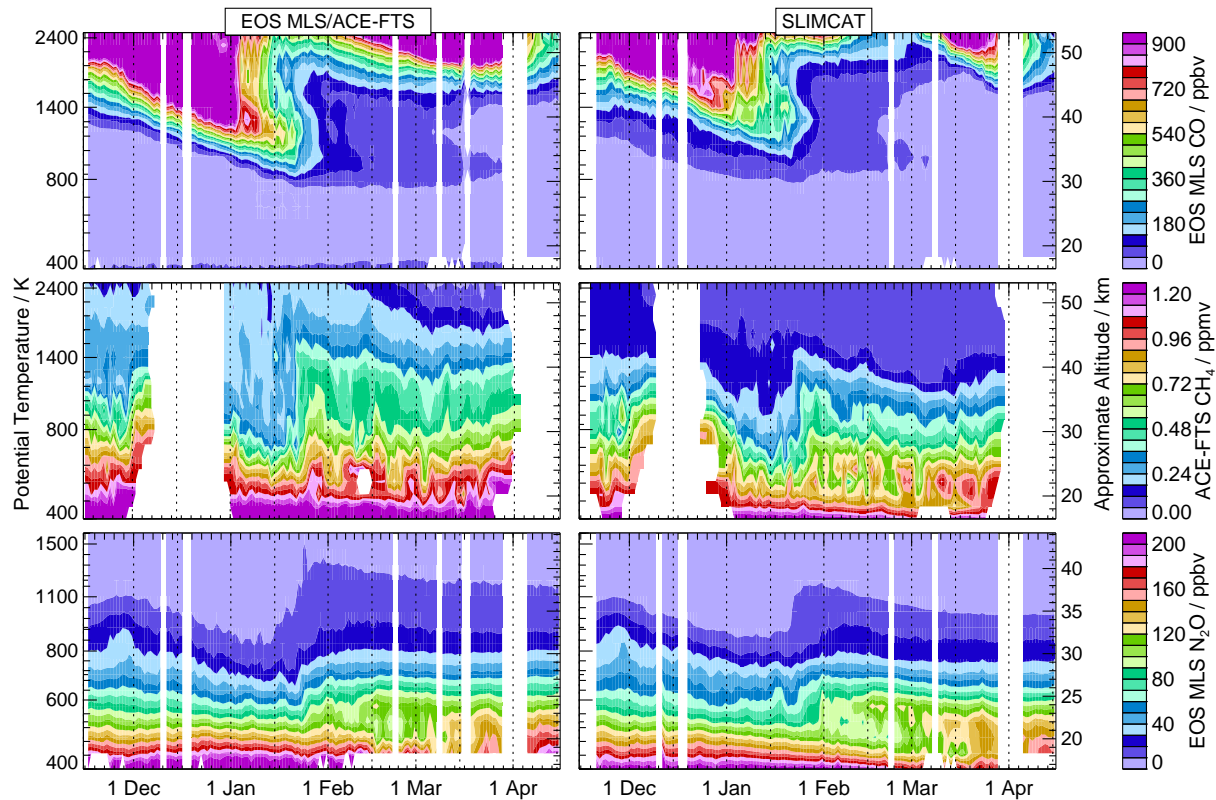


Fig. 5. Vortex averaged (within $1.4 \times 10^{-4} \text{ s}^{-1} \text{ sPV}$ contour) (top to bottom) MLS CO, ACE-FTS CH₄, and MLS N₂O (left) and SLIMCAT simulations (right). Vertical range is from 400 to 2500 K (into the lower mesosphere) for CO and CH₄, but 400 to 1600 K (through the middle stratosphere) for N₂O. SLIMCAT CH₄ is sampled near the ACE observation locations for the average shown here.

CO at 2500 K, near or just above the stratopause. Although MLS data (especially CO) are quite noisy at this level, the agreement in values and time evolution between MLS and ACE-FTS is good, confirming that both datasets provide an unbiased representation of these fields. The patterns of CO time evolution are similar to those at 1700 K (Figure 7), but after the SSW high CO (and, since H₂O decreases with height above the middle to upper stratosphere, low H₂O) completely fills the vortex by mid-February. The patterns in SLIMCAT, however, emphasize the model's increasing inability to capture the transport at higher altitudes after the warming: SLIMCAT shows a period with high H₂O and low CO in the vortex after the SSW, prior to the descent in mid-March of high CO and low H₂O. The period with these dramatically different values in SLIMCAT immediately follows the switch to driving fields with a higher model top (Section 2.4), and thus may be related not only to deficiencies in the contemporaneous transport, but also to vertical transport of values from regions at the top of the ECMWF analyses that had an even poorer representation of earlier transport.

4.2 Discussion: USLM Descent

The dramatic deficiencies in SLIMCAT in the USLM after ~ 5 February suggest either diabatic *ascent* in the model, or the possibility of very inappropriate boundary conditions (the model top is at 3000 K). However, the eventual appearance of a signature of descent by 15 March in SLIMCAT, and the consistency in the anticorrelation between H₂O and CO (e.g., Figure 8), suggest that inaccurate diabatic descent is likely the primary cause of the failure. Figure 9 shows timeseries of 70°N radiative heating rates calculated using MLS and ECMWF temperatures during the 2005–2006 Arctic winter. Modest differences are seen before the SSW, with ECMWF having strongest descent at slightly higher altitudes (near 0.1 hPa), and slightly weaker descent near and below 1 hPa, consistent with the SLIMCAT simulations showing less CO descending through the upper stratosphere in early winter. The most dramatic differences, however, are after the SSW, in February and March. In February, the ECMWF calculation shows dramatically less descent between ~ 0.3 and 0.01 hPa, consistent with the biases in ECMWF temperatures during that period noted by Manney et al. (2008b). The duration of the period of zero descent to weak ascent between

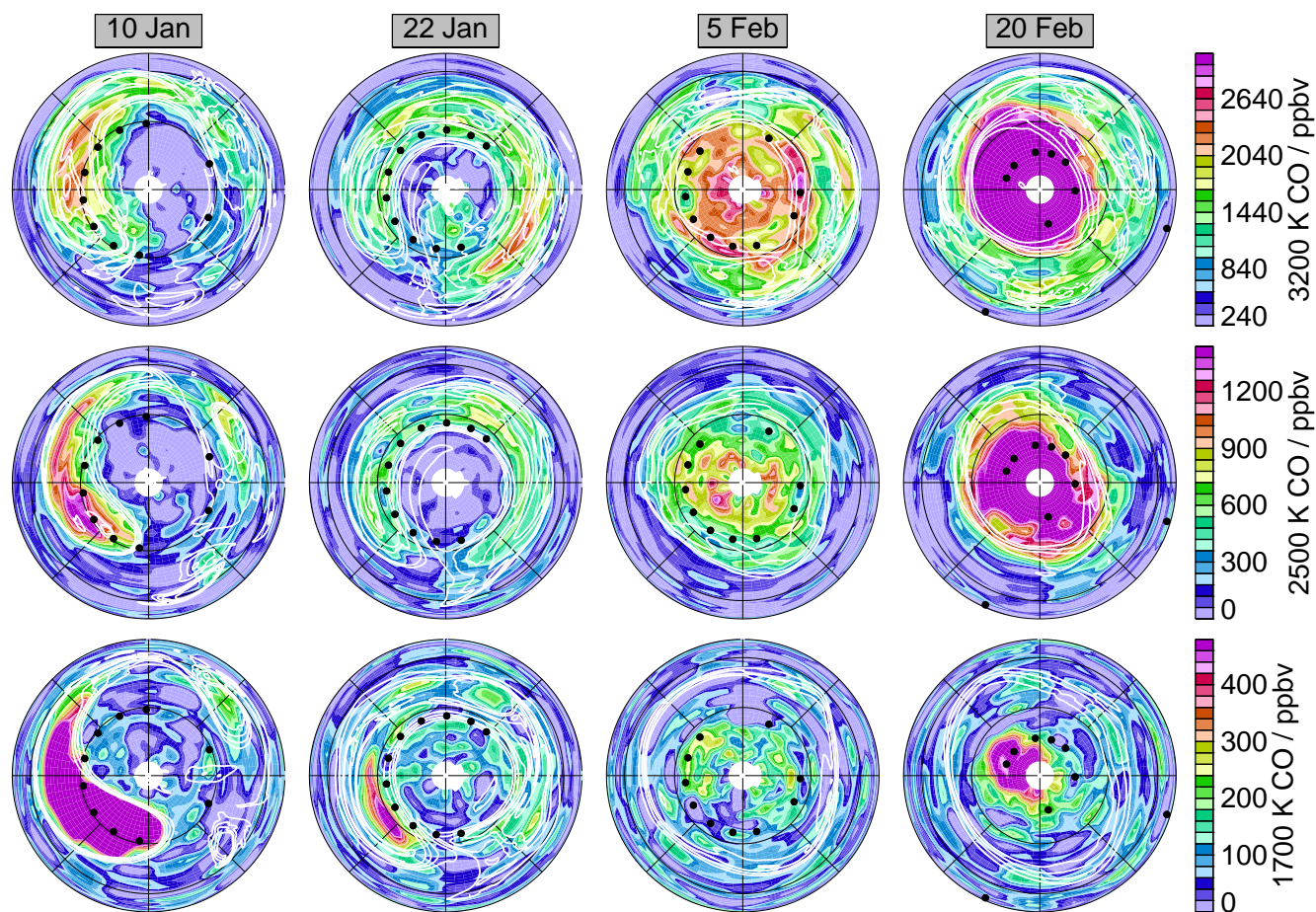


Fig. 6. Maps of MLS CO (ppbv) in the USLM before, during and after the 2006 SSW. Layout and overlays are as in Figure 1.

0.04 and 0.01 hPa in late January is longer in ECMWF- than MLS-derived profiles, and centered at slightly higher altitude. In late March, MLS-based descent rates decrease, becoming considerably less than those from ECMWF. These results are qualitatively consistent with the signatures in SLIMCAT CO and H₂O in the USLM suggesting too weak descent (or even ascent) in February, changing to too strong descent in March.

Manney et al. (2008b) showed that GEOS-5 analyses temperatures were biased such that radiative cooling derived from them was too strong above ~ 0.4 hPa (~ 1800 K in the very cold polar regions in mid-February 2006), and too weak (near-zero descent or ascent) near 1 hPa (~ 1500 K at this time); GEOS-4 temperature structure was similar to that in GEOS-5 (Manney et al., 2008a), thus similar patterns of radiative heating would be expected. Comparison of the time evolution of ACE-FTS, SLIMCAT, and GMI Aura4 (driven by GEOS-4 fields) CH₄ at 1700 and 2500 K and in vortex averages (not shown) indicates that enhanced descent (decreasing CH₄) in the USLM begins earlier and is more rapid in

February in the GMI Aura4 simulation than that indicated by the ACE-FTS data, consistent with the patterns of biases in radiative heating. Examination of GEOS-5 assimilated H₂O (not shown) indicates a similar bias in GEOS-5 transport with more rapid than expected descent in the 1700 to 2500 K region in early February.

The results above offer convincing evidence that the deficiencies in the SLIMCAT simulation in the USLM arise primarily from inaccurate temperatures and hence diabatic descent rates after the SSW. The choice of assimilated meteorological fields used to drive transport models is critical to reproducing observed transport. The MLS and ACE-FTS fields shown here provide the first globally distributed daily long-lived trace gas data to thoroughly test the performance of assimilated winds in transport calculations, especially in the USLM and for extreme events, such as this SSW, that severely challenge the abilities of the assimilation systems and underlying GCMs.

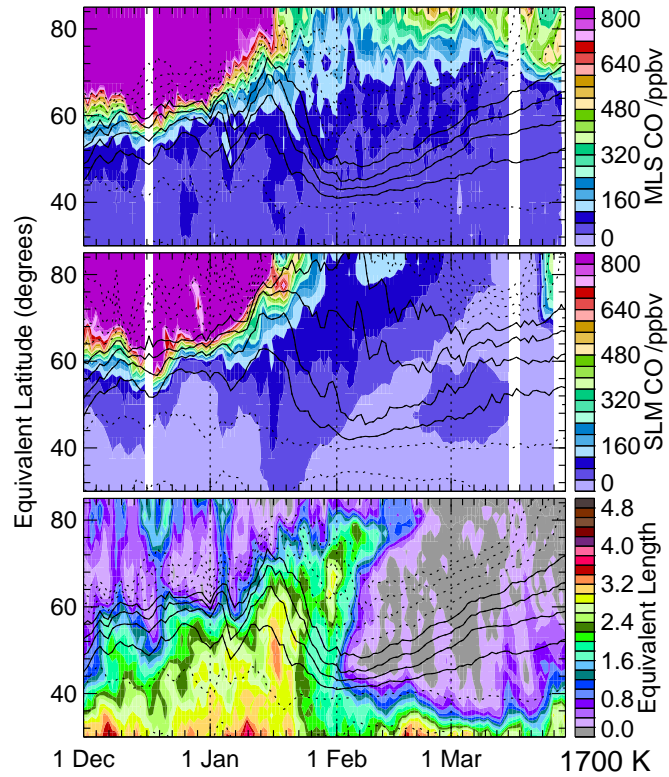


Fig. 7. As in Figure 2, but for MLS (top) and SLIMCAT (center) CO at 1700 K.

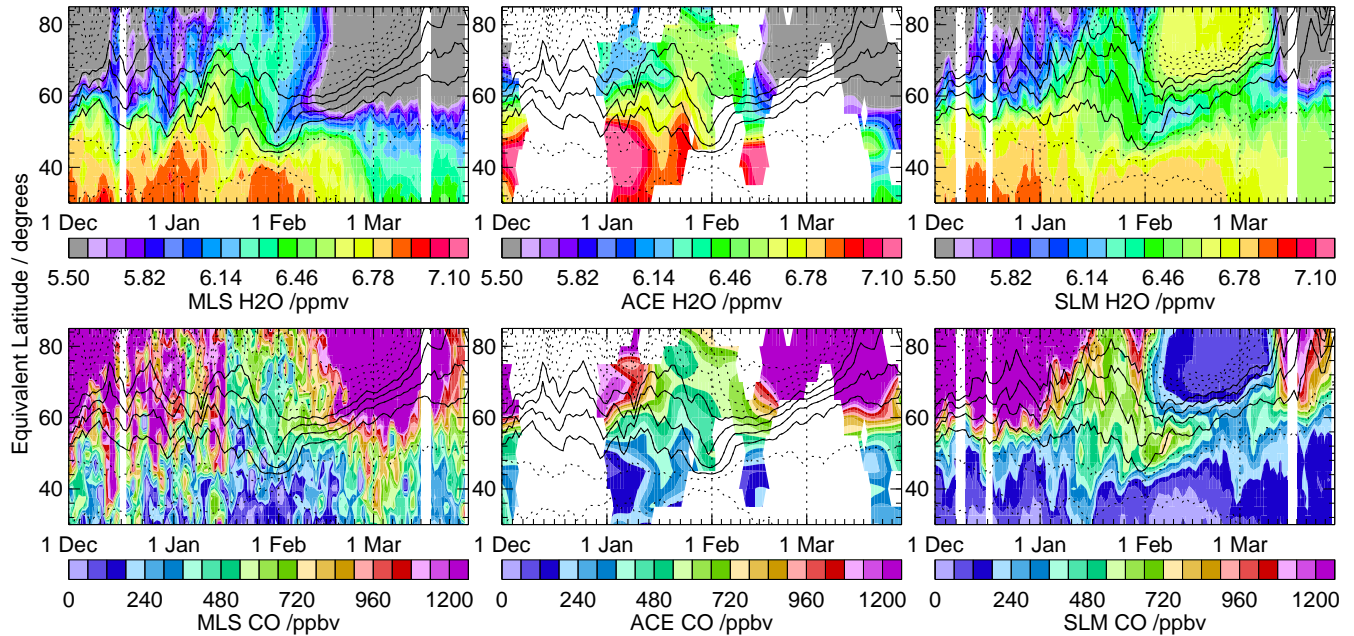


Fig. 8. As in Figure 2, but for (left to right) MLS, ACE-FTS and SLIMCAT H₂O (top) and CO (bottom) on the 2500 K isentropic surface.

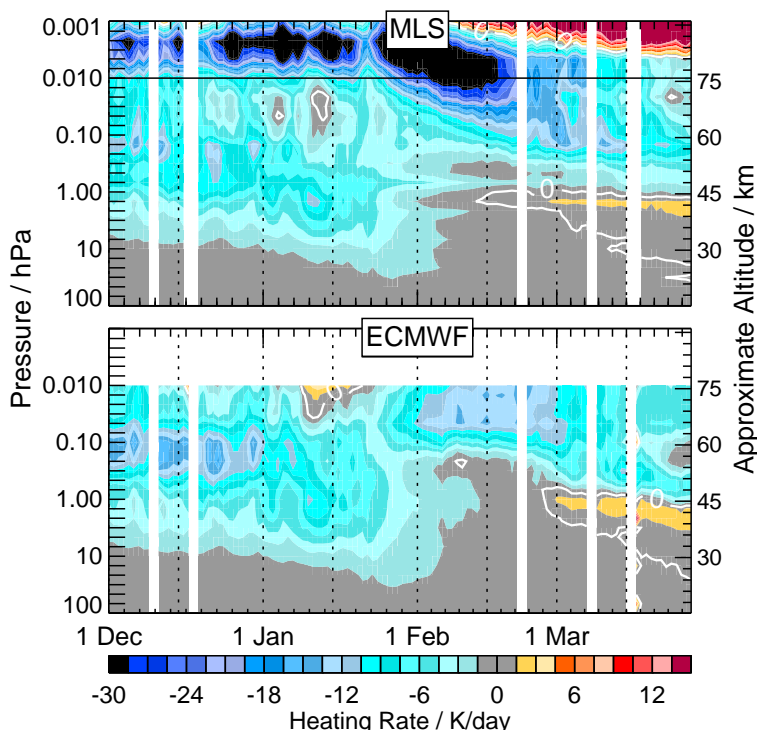


Fig. 9. 70°N zonal mean radiative heating (negative values indicate diabatic descent) rates calculated from MLS (top) and ECMWF (bottom) temperatures (see text for details).

5 The Upper Troposphere/Lower Stratosphere

The MLS (and other Aura instruments, e.g., Olsen et al., 2008) and ACE-FTS (e.g., Hegglin et al., 2008, 2009) datasets also offer the first extensive fields in the upper troposphere and lowermost stratosphere (that portion of the stratosphere below 380 K where isentropes intersect the tropopause, thus lying partly in the troposphere and partly in the stratosphere, Hoskins, 1991; Holton et al., 1995), allowing comprehensive study of UTLS trace gas fields suitable for detailed examination of transport. UTLS dynamics are closely involved in the occurrence and evolution of SSWs. Coy et al. (2008) showed evidence suggesting that propagation of waves originating from a localized upper tropospheric ridge in mid-January was responsible for triggering the 2006 SSW. Keil et al. (2007) showed an episode of extremely low total column O₃ over the UK at this time, resulting from lofting and anomalous poleward transport associated with the originating region of the SSW in the UTLS. The episodes of upper tropospheric ridging, both that implicated in triggering the SSW and later episodes (e.g., Olsen et al., 2008; Coy et al., 2008), are associated with wave propagation that influences the stratospheric/mesospheric flow and hence transport throughout the middle atmosphere.

Several trace gases measured by MLS are useful in the

UTLS; in particular, the morphology and evolution of O₃ and HNO₃ are well-represented (albeit with some biases) in this region (Livesey et al., 2008; Santee et al., 2007, 2009). Figure 10 shows maps at 380 and 350 K from MLS, SLIMCAT, and RT calculations (Section 2.4) on 17–19 January, during the development of the ridge thought to have triggered the SSW. O₃ is shown at 350 K and HNO₃ at 380 K; a consistent picture of the morphology and evolution of the fields is seen between O₃ and HNO₃ at both levels. The MLS fields reveal the effects of transport associated with three evolving ridges, as described below:

The most ridge intense moved from the mid-Atlantic over the Greenwich meridian during the three days shown, intensifying between 17 and 18 January, and moving slightly equatorward by 19 January. This strong ridge was identified by Coy et al. (2008) as the primary source of the waves that propagated into the stratosphere to trigger the 2006 SSW. A sequence of upper tropospheric ridges like this is the signature of a Rossby wave train associated with a blocking event, which is often instrumental in forcing SSWs (e.g., Allen et al., 2006, and references therein). Associated with the mid-Atlantic ridge on 17 January is a large tongue of low-latitude, tropospheric air with low O₃ and HNO₃ drawn up to high latitudes, near 60°N (note that the white tropopause contour is drawn into high latitudes and cut off). This is a deep

feature apparent at both higher and lower levels (down to at least 340 K, near the lower limit of the MLS data, and up to at least 400 K); it sits directly below the area of lowest temperatures in the lower stratosphere, consistent with the characteristic dynamical situation during “ozone mini-hole” events (e.g., Allen and Nakamura, 2002), such as that reported by Keil et al. (2007) at this time.

At 380 K, low O₃ and HNO₃ were transported to high latitudes in conjunction with another strong ridge near 45°E on 17 January, which moved slightly eastward, tilting westward with latitude, and weakened, through 19 January. This ridge was shallower in the vertical and already weakening, thus 350 K fields show low (but not tropospheric) O₃ being drawn into high latitudes on 17 January, but little further poleward transport after that. A third ridge, and accompanying transport of tropospheric air to high latitudes, formed near 270°E on 17 January and subsequently deepened and moved eastward to near 315°E by 19 January. The MLS, SLIMCAT, and RT fields all represent this evolution very similarly. This close agreement demonstrates not only the quality of the MLS data for examining the patterns of UTLS transport, but also argues for high quality in the UTLS of winds from both ECMWF and GEOS-5 (the former driving SLIMCAT, the latter, the RT calculations) winds in the UTLS; these assimilation systems are well constrained by data in the extra-tropical UTLS. The RT fields show fine-scale structure that is not apparent in, or expected to be captured at the resolution of, the MLS and SLIMCAT fields. The veracity of the details of this fine-scale structure are difficult to verify in absence of high-resolution measurements; however, previous studies have verified similar structure in RT calculations during periods with aircraft measurements. A few ACE-FTS profiles (near 60°N on these days) were taken in the region of fine structure, including several along the filament of high HNO₃ seen at 380 K on 17 and 18 January paralleling the southern edge of the high HNO₃ region; examination of these profiles does suggest some fine structure in the vertical that is consistent between several species and similar to that in profile RT calculations at these locations; however, the quality of and resolution realized in individual ACE-FTS profiles at these levels (Hegglin et al., 2008) are not sufficient to say with confidence whether those subtle variations are real.

Examination of fields before (e.g., at least back to 5 January, not shown) and after (e.g., 26 January, 4 February, (Olsen et al., 2008)) the breakdown of the stratospheric vortex indicates that ridges drawing low latitude air up into high latitudes were a common, repeated feature of the circulation during much of the 2005–2006 Arctic winter; during each episode, a ridge in the east Atlantic caused low O₃ and HNO₃ to be drawn into high latitudes (poleward of 60°N), with evidence of quasi-isentropic stratosphere/troposphere exchange in late January and early February (Olsen et al., 2008).

The vertical structure sampled by MLS during this period is shown in Figure 11, which presents cross-sections of MLS

and SLIMCAT O₃ in the UTLS along the MLS orbit tracks shown in Figure 10. Overlaid windspeed contours show the locations of the upper tropospheric and stratospheric jets; the thermal (WMO, temperature gradient) and dynamical ($4.5 \times 10^{-6} \text{ K m}^2 \text{ kg}^{-1} \text{ s}^{-1}$, 4.5 PVU) tropopause locations are also shown. The vertical spacing of the SLIMCAT fields is twice as dense as that for MLS, but they are sampled (and plotted) at the same horizontal locations. The section on the top left shows a track on 17 January that sampled in the midst of the region of low O₃ drawn up to high latitudes; the other tracks are to the west of that region on each day. Both sections shown on 17 January cut across the strong high latitude upper tropospheric jet (the “polar jet”) accompanying the ridge, as well as the subtropical jet (STJ). As is typical (e.g., Holton et al., 1995; Shepherd, 2002), the tropopause drops sharply poleward of the STJ; over the strong ridge (top left sections), it rises abruptly in the vicinity of the polar jet. In all of the sections, strong O₃ gradients correspond closely to the 4.5 PVU dynamical tropopause contour. Double thermal tropopauses are common on the poleward side of the STJ (e.g., Randel et al., 2007), and an extensive region with a double tropopause between the STJ and polar jets is seen in each of the sections to the west of the ridge. On 17 January, the polar jet associated with the ridge lies directly under the stratospheric jet, which defines the southernmost edge of the polar vortex that is shifted off the pole in this direction – the other edge of the vortex is near the pole, and can be identified as the increase in windspeed at the highest latitudes/altitudes shown. On 18 and 19 January, the polar jet has weakened and is largely to the east of the tracks shown (see Figure 10).

Evidence of both tropospheric and stratospheric intrusions is apparent in each of the O₃ fields shown here: On 17 January (top left in Figure 11), O₃ in the area of the ridge had mainly low values characteristic of the troposphere, but a large tongue with stratospheric O₃ values extended down and poleward between the STJ and polar jet, resulting in a layered structure with tropospheric O₃ values above stratospheric ones. The other sections, taken west of the ridge, have a layer with tropospheric O₃ values extending northeastward along the orbit in the region with a double tropopause. Characteristically lower UTLS O₃ in profiles with a double tropopause, with a notched profile above the primary (lowest altitude) tropopause (e.g., Randel et al., 2007) arises from patterns of O₃ transport like those shown here. Despite its coarse vertical resolution (the y-axis tick marks show every retrieval level), most such features seen in the SLIMCAT simulations are represented to some extent in the MLS sections. Because of the coarse spacing, capturing such features can be somewhat fortuitous in MLS, and in SLIMCAT may depend on even small inaccuracies in the driving wind fields that may result in small offsets in the position of modelled features. In some cases (e.g., top left track on 17 January, greater latitudinal extent of high O₃ feature), the MLS profiles contain structure that is not as obvious in the SLIMCAT sections, while in other cases (especially intrusions of low O₃ on 18

and 19 January), MLS shows a coarser-grain picture of the features seen in SLIMCAT. Olsen et al. (2008) presented a similar analysis of Aura High Resolution Dynamics Limb Sounder (HIRDLS) data and GMI Aura4 simulation results for 26 January through 4 February; HIRDLS has considerably better vertical resolution than MLS, and the orbit tracks are offset between the two instruments. Nevertheless, examination of MLS and SLIMCAT sections on those days (not shown) indicates that MLS captures similar behavior. That both GMI and SLIMCAT (driven by GEOS-4 and ECMWF winds, respectively) accurately represent this UTLS structure is indicative of the high quality of the assimilated meteorological analyses that drive the simulations in the UTLS.

Figure 12 shows O_3 from MLS and SLIMCAT along with K_{eff} at 380 and 350 K; although at these levels EqL is becoming less appropriate as a “zonal” coordinate since a single circumpolar jet is less representative of the flow (see Figure 10), these still provide a summary of the average time evolution in a framework consistent with that shown at higher levels (e.g., Figures 2, 3). At 350 K, the 4.5 PVU contour corresponds to the minimum in K_{eff} , and MLS and SLIMCAT fields (as well as ACE-FTS, not shown) show very strong O_3 gradients across the 4.5 PVU contour, indicating that this contour is an accurate identification of the tropopause as a transport barrier in the EqL average. At 380 K, the strongest transport barrier and O_3 gradients are at higher EqLs than the 4.5 PVU contour. 380 K is the level typically defined as the top boundary of the lowermost stratosphere (e.g., Hoskins, 1991). This transport barrier is thus above the classical definition of the tropopause, and transport with respect to it is determined by the transport characteristics within the tropically controlled transition region (between ~ 380 and ~ 420 K, Rosenlof et al., 1997) where a distinct seasonality in mixing strength between the tropics and extratropics has been observed. (Hegglin and Shepherd, 2007). As shown by Haynes and Shuckburgh (2000b) and Allen and Nakamura (2001), the strength of mixing barriers is strongly correlated with the strength of the zonal wind, with higher (lower) windspeeds corresponding to lower (higher) K_{eff} values. At 350 K, the strongest winds are associated with the upper tropospheric subtropical jet (STJ), which is nearly continuous around the globe near 30° latitude, coincident with the location of the 4.5 PVU contour at that level (see Figure 10). In contrast, the STJ does not extend up to 380 K at all longitudes, thus at many locations, the strongest winds are associated with the upper tropospheric polar jet and the lowermost extension of the polar night jet (which are both at higher latitudes, near 60°N , and correspond to higher PV values); the low K_{eff} region seen at 380 K is indicative of a transport barrier that varies in strength and location with longitude, and is not always representative of the tropopause level. (Larger K_{eff} at low latitudes at 380 K may be related to the zero zonal wind line being shifted north of the equator, where waves breaking along the critical line may cause significant material mixing; Plumb and Mahlman (1987).)

At both levels, episodic poleward extension of the low K_{eff} representing a strong transport barrier is seen starting in late December and continuing into early February – these are the signatures in the EqL average of the local episodes of elevated tropopauses seen in the maps and curtains shown above, which correspond to regions where the STJ is weak and the upper tropospheric polar jet lies directly under the bottom of the stratospheric polar night jet. As apparent in Figure 10, these episodes are associated with poleward transport of low O_3 at the longitudes of the ridges. Because of the complexity of the jet structure (and hence PV and EqL fields) at these levels, the EqL coordinate is not as effective at separating different air masses as in the stratosphere. However, a hint of the poleward transport can be seen in the O_3 fields at 380 and 350 K (especially 350 K in early February). Comparison with the time evolution at 520 K in the lower stratosphere (e.g., Figures 1 and 3) shows a signature of poleward transport outside the vortex in early January that is consistent in MLS, ACE-FTS (not shown) and SLIMCAT, and occurs over the region of elevated tropopause. The deep region of anomalous poleward transport outside the vortex associated with the event implicated in forcing the SSW (Coy et al., 2008) thus extends well into the lower stratosphere. The primary feature of note in the general time evolution of 350 and 380 K O_3 is the increase in O_3 via diabatic descent. At 380 K, the tightening of PV contours beginning before mid January, and the appearance of confinement of O_3 within these contours (stronger O_3 gradients), suggests some influence of the stratospheric vortex extending into the lowermost stratosphere, albeit with less distinct confinement than at higher levels. There appears to be an accelerated increase in O_3 in the polar regions at both levels in mid to late January, likely related to the increasingly disturbed and warming vortex above, which is associated with enhanced diabatic descent as the temperatures depart farther from radiative equilibrium.

6 Summary and Conclusions

The January 2006 event was the first major SSW for which globally distributed long-lived trace gas data are available covering the lowermost stratosphere through the lower mesosphere. It was also one of the strongest and most prolonged SSWs on record. We have used Aura MLS data, augmented by fields from ACE-FTS, along with a state-of-the-art CTM and assimilated meteorological analyses, to detail three dimensional transport from the UTLS through the USLM during the 2006 SSW, and to help assess the consistency of dynamical fields from operational assimilation systems with the observed transport. Figure 13 summarizes the evolution of the SSW in relation to transport reflected in the MLS data.

The SSW was apparently triggered by waves propagating upward from a strong upper tropospheric ridge just after mid-January (Coy et al., 2008). This ridge was accompa-

nied by an elevated tropopause, and strong poleward transport in a deep region of the UTLS, at some levels leading to quasi-isentropic stratosphere/troposphere exchange. MLS trace gases in the UTLS show a deep layer extending from below the tropopause through the lower stratosphere with enhanced poleward transport of low O_3 and HNO_3 outside the vortex. These patterns of transport result in lamination in the trace gases in the levels around the tropopause, typically in a region with a double tropopause, resulting from both intrusions of stratospheric air into the troposphere and tropospheric air into the stratosphere.

The stratospheric vortex broke apart from the top down, with K_{eff} calculations showing the complete disappearance of the polar vortex transport barrier in the upper stratosphere just after mid-January, and by late January in the middle stratosphere. At these levels, the vortex breakdown was very rapid, occurring over a few days. The evolution of PV and the K_{eff} calculations show a somewhat more gradual and later breakdown in the lower stratosphere, with the transport barrier shrinking to a small area in mid-February. K_{eff} , and the trace gas evolution, shows a small remnant of the vortex persisting throughout the winter below the middle stratosphere (~ 850 K and below).

Consistent with the disappearance of the transport barrier, trace gases measured by MLS (CO and H_2O , and N_2O in/below the middle stratosphere) and ACE-FTS show the signature of strong mixing, with values characteristic of low and midlatitudes extending to the polar regions and extremely weak tracer gradients throughout the hemisphere. In the middle and lower stratosphere, small remnants with high H_2O /low N_2O values characteristic of the pre-SSW vortex lingered into the recovery.

In the upper stratosphere to lower mesosphere, the vortex very quickly reformed and strengthened, becoming larger and stronger than before the SSW by early February. High-vortex CO existing before the warming from the mesosphere down to the middle stratosphere was mixed with lower latitude air with orders of magnitude less CO , resulting in very low CO at all latitudes during the SSW. As the vortex reformed and very strong diabatic descent developed (e.g., Siskind et al., 2007; Manney et al., 2008b), high CO was once again transported from the mesosphere into the confined upper stratospheric vortex, echoing the pattern of descent typically seen in fall/early winter.

In the middle and lower stratosphere the vortex and transport barrier remained weak after the SSW for the duration of the winter. Trace gas gradients remained correspondingly weak, with (especially in the lower stratosphere) lingering small vortex remnants with pre-SSW trace gas values enclosed within a larger region of weak, but distinct, gradients associated with the weak reformed vortex.

The evolution of the trace gas distributions is consistent with that of the dynamical fields (PV, K_{eff}) in meteorological analyses shown here, with agreement being somewhat weaker in the upper stratosphere/lower mesosphere in the pe-

riod after the SSW, consistent with deficiencies reported by Manney et al. (2008b) in the operational assimilated analyses during that period.

The SLIMCAT CTM, driven by ECMWF winds, also does a very good job of simulating transport during the SSW in the UTLS through the middle stratosphere, with differences only in detail, such as slightly too strong descent in the lower stratosphere, and not quite enough mixing in the middle stratosphere. In the upper stratosphere and lower mesosphere, however, the SLIMCAT simulation failed to capture the strong descent of mesospheric CO and H_2O values into the reformed vortex. The descent is seen to begin much later than that observed, and at that point becomes too strong. Radiation calculations based on MLS versus ECMWF temperatures show that strong biases in ECMWF temperatures result in much weaker descent immediately after the SSW, followed by descent becoming stronger than that derived from MLS temperatures about a month later. This pattern is consistent with the most obvious failings of the SLIMCAT simulation in the USLM. These deficiencies in the USLM may be exacerbated by the proximity of this region to the model top and by differences in the vortex structure/horizontal winds at these levels. A simulation with a different CTM driven with GEOS-4 winds (which have opposite temperature biases to ECMWF in the period following the SSW) shows too rapid descent into the vortex following the SSW. Thus, the evidence indicates that the failings of CTMs in the upper stratosphere result primarily from corresponding inaccuracies in the wind and, especially, temperature fields used to drive them.

The above results provide the first detailed, comprehensive observational picture of transport during a major SSW covering the upper troposphere throughout the lower mesosphere, and an assessment of the representation of that transport in a state-of-the-art CTM. Recent satellite datasets, such as the MLS and ACE-FTS data used here, are critical to such assessments, which in turn are essential to improving our data assimilation and modelling capabilities.

Acknowledgements. Thanks to the MLS team, especially Lucien Froidevaux, Brian W. Knosp, and Robert P. Thurstans, and the ACE Team, especially Sean McLeod and Ryan Hughes, for their continuing support and assistance. Thanks to the GMAO and ECMWF for producing/providing their assimilated data products, and to Steven Pawson for helpful discussions and comments; thanks to Susan E. Strahan for making available and providing advice on the GMI Aura4 simulation, and to Martyn Chipperfield for the SLIMCAT model. Research at the Jet Propulsion Laboratory, California Institute of Technology, was done under contract with the National Aeronautics and Space Administration. Funding for the ACE mission was provided primarily by the Canadian Space Agency and the Natural Sciences and Engineering Research Council of Canada. Ian MacKenzie is funded by the UK Natural Environment Research Council.

References

- Allen, D. R. and Nakamura, N.: A seasonal climatology of effective diffusivity in the stratosphere, *J. Geophys. Res.*, 106, 7917–7935, 2001.
- Allen, D. R. and Nakamura, N.: Dynamical reconstruction of the record low column ozone over Europe on 30 November 1999, *Geophys. Res. Lett.*, 29, doi:10.1029/2002GL014935, 2002.
- Allen, D. R., Stanford, J. L., López-Valverde, M. A., Nakamura, N., Lary, D. J., Douglass, A. R., Cerniglia, M. C., Remedios, J. J., and Taylor, F. W.: Observations of middle atmosphere CO from the UARS ISAMS during the early northern winter 1991/1992, *J. Atmos. Sci.*, 56, 563–583, 1999.
- Allen, D. R., Stanford, J. L., Nakamura, N., López-Valverde, M. A., López-Puertas, M., Taylor, F. W., and Remedios, J. J.: Antarctic polar descent and planetary wave activity observed in ISAMS CO from April to July 1992, *Geophys. Res. Lett.*, 27, 665–668, 2000.
- Allen, D. R., Coy, L., Eckermann, S. D., McCormack, J. P., Manney, G. L., Hogan, T. F., and Kim, Y.-J.: NOGAPS-ALPHA Simulations of the 2002 Southern Hemisphere Major Warming, *Mon. Weather Rev.*, 134, 498–518, 2006.
- Bernath, P. F. et al.: Atmospheric Chemistry Experiment (ACE): mission overview, *Geophys. Res. Lett.*, 32, L15S01, doi:10.1029/2005GL022386, 2005.
- Bloom, S. C., Takacs, L. L., da Silva, A. M., and Ledvina, D.: Data Assimilation Using Incremental Analysis Updates, *Mon. Weather Rev.*, 124, 1256–1271, 1996.
- Bloom, S. C. et al.: The Goddard Earth Observing Data Assimilation System, GEOS DAS Version 4.0.3: Documentation and Validation, Tech. Rep. 104606 V26, NASA, 2005.
- Boone, C. D., Nassar, R., Walker, K. A., Rochon, Y., McLeod, S. D., Rinsland, C. P., and Bernath, P. F.: Retrievals for the Atmospheric Chemistry Experiment Fourier-Transform Spectrometer, *Appl. Opt.*, 44, 7218–7231, 2005.
- Braathen, G. et al.: Joint WMO/EU Arctic ozone bulletin, winter/spring summary, Tech. Rep. 2006-1, World Meteorological Organization/European Ozone Research Coordinating Unit, available at <http://www.wmo.int/pages/prog/arep/gaw/ozone/index.html>, 2006.
- Briegleb, B. P.: Delta-Eddington approximation for solar radiation in the NCAR Community Climate Model, *J. Geophys. Res.*, 97, 7603–7612, 1992a.
- Briegleb, B. P.: Longwave band model for thermal radiation in climate studies, *J. Geophys. Res.*, 97, 11,475–11,485, 1992b.
- Carleer, M. et al.: Validation of Water vapor profiles from the Atmospheric Chemistry Experiment (ACE), *Atmos. Chem. Phys. Disc.*, 8, 4499–4559, 2008.
- Chipperfield, M. P.: Multiannual simulations with a three-dimensional chemical transport model, *J. Geophys. Res.*, 104, 1781–1805, 1999.
- Chipperfield, M. P.: New version of the TOMCAT/SLIMCAT offline chemical transport model: Intercomparison of stratospheric tracer experiments, *Q. J. R. Meteorol. Soc.*, 132, 1179–1203, 2006.
- Chipperfield, M. P., Lee, A. M., and Pyle, J. A.: Model calculations of ozone depletion in the Arctic polar vortex for 1991/92 to 1994/95, *Geophys. Res. Lett.*, 23, 559–562, 1996.
- Clerbaux, C., George, M., Turquety, S., et al.: CO measurements from the ACE-FTS satellite instrument: data analysis and validation using ground-based, airborne and spaceborne observations, *Atmos. Chem. Phys.*, 8, 2569–2594, 2008.
- Coy, L., Eckermann, S., and Hoppel, K.: Planetary wave breaking and tropospheric forcing as seen in the stratospheric sudden warming of 2006, *J. Atmos. Sci.*, in press, 2008.
- De Maziere, M. et al.: Validation of ACE v2.2 methane profiles from the upper troposphere to lower mesosphere, *Atmos. Chem. Phys.*, 8, 2421–2435, 2008.
- Dupuy, E. et al.: Validation of ozone measurements from the Atmospheric Chemistry Experiment (ACE), *Atmos. Chem. Phys. Disc.*, 8, 2513–1656, 2008.
- Fairlie, T. D. A., Fisher, M., and O'Neill, A.: The development of narrow baroclinic zones and other small-scale structure in the stratosphere during simulated major warmings, *Q. J. R. Meteorol. Soc.*, 116, 287–315, 1990.
- Feng, W., Chipperfield, M. P., Roscoe, H. K., Remedios, J. J., Waterfall, A. M., Stiller, G. P., Glatthor, N., Höpfner, M., and Wang, D.-Y.: Three-dimensional model study of the Antarctic ozone hole in 2002 and comparison with 2000, *J. Atmos. Sci.*, 62, 822–837, 2005.
- Fisher, M., O'Neill, A., and Sutton, R.: Rapid descent of mesospheric air into the stratospheric polar vortex, *Geophys. Res. Lett.*, 20, 1267–1270, 1993.
- Flocke, F. et al.: An examination of chemistry and transport processes in the tropical lower stratosphere using observations of long-lived and short-lived compounds obtained during STRAT and POLARIS, *J. Geophys. Res.*, 104, 26,625–26,642, 1999.
- Froidevaux, L. et al.: Validation of EOS MLS stratospheric ozone measurements, *J. Geophys. Res.*, 113, D15S20, doi:10.1029/2007JD008771, 2008.
- Haynes, P. and Shuckburgh, E.: Effective diffusivity as a diagnostic of atmospheric transport 1. Stratosphere, *J. Geophys. Res.*, 105, 22,777–22,794, 2000a.
- Haynes, P. and Shuckburgh, E.: Effective diffusivity as a diagnostic of atmospheric transport 2. Troposphere and lower stratosphere, *J. Geophys. Res.*, 105, 22,795–22,810, 2000b.
- Hegglin, M. I. and Shepherd, T. G.: O₃-N₂O correlations from the Atmospheric Chemistry Experiment: Revisiting a diagnostic of transport and chemistry in the stratosphere, *J. Geophys. Res.*, 112, D19301, doi:10.1029/2006JD008281, 2007.
- Hegglin, M. I., Boone, C. D., Manney, G. L., Shepherd, T. G., Walker, K. A., Bernath, P. F., Daffer, W. H., Hoor, P., and Schiller, C.: Validation of ACE-FTS satellite data in the upper troposphere/lower stratosphere (UTLS) using non-coincident measurements, *Atmos. Chem. Phys.*, 8, 1483–1499, 2008.
- Hegglin, M. I., Boone, C. D., Manney, G. L., and Walker, K. A.: A global view of the extratropical tropopause transition layer (ExTL) from Atmospheric Chemistry Experiment Fourier Transform Spectrometer O₃, H₂O, and CO, *J. Geophys. Res.*, 114, in press, 2009.
- Hoffmann, P., Singer, W., Keuer, D., Hocking, W. K., Kunze, M., and Murayama, Y.: Latitudinal and longitudinal variability of mesospheric winds and temperatures during stratospheric warming events, *J. Atmos. Sol.-Ter. Phys.*, 69, 2355–2366, 2007.
- Holton, J. R., Haynes, P. H., McIntyre, M. E., Douglass, A. R., Rood, R. B., and Pfister, L.: Stratosphere-Troposphere exchange, *Rev. Geophys.*, 33, 403–439, 1995.
- Hoskins, B. J.: Towards a PV- θ view of the general circulation,

- Tellus, 43AB, 27–35, 1991.
- Jin, J. J. et al.: Comparison of CMAM simulations of carbon monoxide (CO), nitrous oxide (N₂O), and methane (CH₄) with observations from Odin/SMR, ACE-FTS, and Aura/MLS, *Atmos. Chem. Phys. Disc.*, 8, 13,063–13,123, 2008.
- Keil, M., Jackson, D. R., and Hort, M. C.: The January 2006 low ozone event over the UK, *Atmos. Chem. Phys.*, 7, 961–972, 2007.
- Konopka, P., Groß, J.-U., Hoppel, K. W., Steinhilber, H.-M., and Müller, R.: Mixing and chemical ozone loss during and after the Antarctic polar vortex major warming in September 2002, *J. Atmos. Sci.*, 62, 848–859, 2005.
- Lahoz, W. A. et al.: Three-dimensional evolution of water vapour distributions in the northern hemisphere stratosphere as observed by the Microwave Limb Sounder, *J. Atmos. Sci.*, 51, 2914–2930, 1994.
- Lambert, A. et al.: Validation of the Aura Microwave Limb Sounder stratospheric water vapor and nitrous oxide measurements, *J. Geophys. Res.*, 113, D24S36, doi:10.1029/2007JD008724, 2007.
- Leovy, C. B., Sun, C., Hitchman, M. H., Remsberg, E. E., Russell, III, J. M., Gordley, L. L., Gille, J. C., and Lyjak, L. V.: Transport of ozone in the middle stratosphere: Evidence for planetary wave breaking, *J. Atmos. Sci.*, 42, 230–244, 1985.
- Livesey, N. J. et al.: MLS Version 2.2 Level 2 data quality and description document, Tech. Rep. JPL D-33509, Jet Propulsion Laboratory, available at <http://mls.jpl.nasa.gov>, 2007.
- Livesey, N. J. et al.: Validation of Aura Microwave Limb Sounder O₃ and CO observations in the upper troposphere and lower stratosphere, *J. Geophys. Res.*, 113, D15S02, doi:10.1029/2007JD008805, 2008.
- Manney, G. L., Farrara, J. D., and Mechoso, C. R.: Simulations of the February 1979 stratospheric sudden warming: Model comparisons and three-dimensional evolution, *Mon. Weather Rev.*, 122, 1115–1140, 1994a.
- Manney, G. L., Zurek, R. W., O'Neill, A., and Swinbank, R.: On the motion of air through the stratospheric polar vortex, *J. Atmos. Sci.*, 51, 2973–2994, 1994b.
- Manney, G. L., Zurek, R. W., O'Neill, A., Swinbank, R., Kumer, J. B., Mergenthaler, J. L., and Roche, A. E.: Stratospheric warmings during February and March 1993, *Geophys. Res. Lett.*, 21, 813–816, 1994c.
- Manney, G. L., Froidevaux, L., Waters, J. W., Gille, J. C., Zurek, R. W., Kumer, J. B., Mergenthaler, J. L., Roche, A. E., O'Neill, A., and Swinbank, R.: Formation of low-ozone pockets in the middle stratospheric anticyclone during winter, *J. Geophys. Res.*, 100, 13,939–13,950, 1995.
- Manney, G. L., Bird, J. C., Donovan, D. P., Duck, T. J., Whiteway, J. A., Pal, S. R., and Carswell, A. I.: Modeling ozone laminae in ground-based Arctic wintertime observations using trajectory calculations and satellite data, *J. Geophys. Res.*, 103, 5797–5814, 1998.
- Manney, G. L., Lahoz, W. A., Swinbank, R., O'Neill, A., Connew, P. M., and Zurek, R. W.: Simulation of the December 1998 stratospheric major warming, *Geophys. Res. Lett.*, 26, 2733–2736, 1999a.
- Manney, G. L., Michelsen, H. A., Santee, M. L., Gunson, M. R., Irion, F. W., Roche, A. E., and Livesey, N. J.: Polar vortex dynamics during spring and fall diagnosed using trace gas observations from the Atmospheric Trace Molecule Spectroscopy instrument, *J. Geophys. Res.*, 104, 18,841–18,866, 1999b.
- Manney, G. L., Krüger, K., Sabutis, J. L., Sena, S. A., and Pawson, S.: The remarkable 2003–2004 winter and other recent warm winters in the Arctic stratosphere since the late 1990s, *J. Geophys. Res.*, 110, D04107, doi:10.1029/2004JD005367, 2005a.
- Manney, G. L., Sabutis, J. L., Allen, D. R., Lahoz, W. A., Scaife, A. A., Randall, C. E., Pawson, S., Naujokat, B., and Swinbank, R.: Simulations of dynamics and transport during the September 2002 Antarctic major warming, *J. Atmos. Sci.*, 62, 690–707, 2005b.
- Manney, G. L. et al.: Solar Occultation Satellite Data and Derived Meteorological Products: Sampling Issues and Comparisons with Aura MLS, *J. Geophys. Res.*, 112, D24S50, doi:10.1029/2007JD008709, 2007.
- Manney, G. L. et al.: The High Arctic in Extreme Winters: Vortex, Temperature, and MLS Trace Gas Evolution, *Atmos. Chem. Phys.*, 8, 505–522, 2008a.
- Manney, G. L. et al.: The evolution of the stratopause during the 2006 major warming: Satellite Data and Assimilated Meteorological Analyses, *J. Geophys. Res.*, 113, D11115, doi:10.1029/2007JD009097, 2008b.
- Minschwaner, K., Carver, R. W., Briegleb, B. P., and Roche, A. E.: Infrared radiative forcing and atmospheric lifetimes of trace species based on observations from UARS, *J. Geophys. Res.*, 103, 23,243–23,253, 1998.
- Olsen, M. A., Douglass, A. R., Newman, P. A., Gille, J. C., Nardi, B., Yudin, V. A., Kinnison, D. E., and Khosravi, R.: HIRDLS observations and simulation of a lower stratospheric intrusion of tropical air to high latitudes, *Geophys. Res. Lett.*, 35, L21813, doi:10.1029/2008GL035514, 2008.
- O'Neill, A., Grose, W. L., Pope, V. D., McClean, H., and Swinbank, R.: Evolution of the stratosphere during northern winter 1991/92 as diagnosed from U.K. Meteorological Office analyses, *J. Atmos. Sci.*, 51, 2800–2817, 1994.
- Plumb, R. A. and Mahlman, J. D.: The zonally averaged transport characteristics of the GFDL general circulation/transport model, *J. Atmos. Sci.*, 44, 298–327, 1987.
- Pumphrey, H. C. et al.: Validation of the Aura Microwave Limb Sounder stratospheric and mesospheric CO measurements, *J. Geophys. Res.*, 112, D24S38, doi:10.1029/2007JD008723, 2007.
- Randall, C. E., Manney, G. L., Allen, D. R., Bevilacqua, R. M., Trepte, C., Lahoz, W. A., and O'Neill, A.: Reconstruction and Simulation of Stratospheric Ozone Distributions During the 2002 Austral Winter, *J. Atmos. Sci.*, 62, 748–764, 2005.
- Randall, C. E., Harvey, V. L., Singleton, C. S., Bernath, P. F., Boone, C. D., and Kozyra, J. U.: Enhanced NO_x in 2006 linked to strong upper stratospheric Arctic vortex, *Geophys. Res. Lett.*, 33, L18811, doi:10.1029/2006GL027160, 2006.
- Randel, W. J., Seidel, D. J., and Pan, L.: Observational characteristics of double tropopauses, *J. Geophys. Res.*, 112, D07309, doi:10.1029/2006JD00794, 2007.
- Reinecker, M. M. et al.: The GEOS-5 Data Assimilation System: A Documentation of GEOS-5.0, Tech. Rep. 104606 V27, NASA, 2008.
- Rosenlof, K. H., Tuck, A. F., Kelly, K. K., III, J. M. R., and McCormick, M. P.: Hemispheric asymmetries in water vapor and inferences about transport in the lower stratosphere, *J. Geophys. Res.*, 103, 15,189–15,200, 1998.

- Res., 102, 13, 213–213, 234, 1997. 1485
- Santee, M. L., Manney, G. L., Froidevaux, L., Read, W. G., Livesey, N. J., and Lambert, A.: Trace gas evolution in the lowermost stratosphere from Aura Microwave Limb Sounder measurements: Subvortex processing and transport, *J. Geophys. Res.*, to be submitted, 2009. 1490
- Santee, M. L. et al.: Validation of the Aura Microwave Limb Sounder HNO₃ measurements, *J. Geophys. Res.*, 112, D24S40, doi:10.1029/2007JD008721, 2007.
- Santee, M. L. et al.: A study of stratospheric chlorine partitioning based on new satellite measurements and modeling, *J. Geophys. Res.*, 113, D12307, doi:10.1029/2007JD009057, 2008. 1435
- Schwartz, M. J. et al.: Validation of the Aura Microwave Limb Sounder temperature and geopotential height measurements, *J. Geophys. Res.*, 113, D15S11, doi:10.1029/2007JD008783, 2008. 1440
- Shepherd, T. G.: Issues in stratosphere-troposphere coupling, *J. Meteor. Soc. Japan*, 80, 769–792, 2002.
- Shepherd, T. G.: Transport in the middle atmosphere, *J. Meteorol. Soc. Japan*, 85B, 165–191, 2007. 1445
- Shepherd, T. G.: Dynamics, Stratospheric Ozone, and Climate Change, *Atmosphere-Ocean*, 46, 371–392, 2008.
- Simmons, A. J., Hortal, M., Kelly, G., McNally, A., Untch, A., and Uppala, S.: ECMWF analyses and forecasts of stratospheric winter polar vortex break-up: September 2002 in the southern hemisphere and related events, *J. Atmos. Sci.*, 62, 668–689, 2005. 1450
- Siskind, D. E., Eckermann, S. D., Coy, L., and McCormack, J. P.: On recent interannual variability of the Arctic winter mesosphere: Implications for tracer descent, *Geophys. Res. Lett.*, 34, L09806, doi:10.1029/2007GL029293, 2007. 1455
- Strahan, S. E., Duncan, B. N., and Hoor, P.: Observationally derived transport diagnostics for the lowermost stratosphere and their application to the GMI chemistry and transport model, *Atmos. Chem. Phys.*, 7, 2435–2445, 2007.
- Strong, K. et al.: Validation of ACE-FTS N₂O measurements, *Atmos. Chem. Phys.*, 8, 4759–4786, 2008. 1460
- Sutton, R. T., MacLean, H., Swinbank, R., O'Neill, A., and Taylor, F. W.: High-resolution stratospheric tracer fields estimated from satellite observations using Lagrangian trajectory calculations, *J. Atmos. Sci.*, 51, 2995–3005, 1994. 1465
- Swinbank, R. and O'Neill, A.: A stratosphere-troposphere data assimilation system, *Mon. Weather Rev.*, 122, 686–702, 1994.
- Swinbank, R., Ingleby, N. B., Boorman, P. M., and Renshaw, R. J.: A 3D variational data assimilation system for the stratosphere and troposphere, *Tech. Rep. 71*, Met Office Numerical Weather Prediction Forecasting Research Scientific Paper, 2002. 1470
- Swinbank, R., Keil, M., Jackson, D. R., and Scaife, A. A.: Stratospheric Data Assimilation at the Met Office - progress and plans, in: ECMWF workshop on Modelling and Assimilation for the Stratosphere and Tropopause 23–26 June, 2003, ECMWF, 2004. 1475
- Tan, W. W., Geller, M. A., Pawson, S., and da Silva, A.: A case study of excessive subtropical transport in the stratosphere of a data assimilation system, *J. Geophys. Res.*, 109, D11102, doi:10.1029/2003JD004057, 2004.
- Untch, A., Miller, M., Hortal, M., Buizza, R., and Janssen, P.: Towards a global meso-scale model: The high resolution system T799L91 and T399L62 EPS, *ECMWF Newsletter*, 108, 6–13, 2006. 1480
- Waters, J. W. et al.: The Earth Observing System Microwave Limb Sounder (EOS MLS) on the Aura satellite, *IEEE Trans. Geosci. Remote Sens.*, 44, 1075–1092, 2006.
- WMO: Scientific assessment of stratospheric ozone depletion: 2006, U. N. Environ. Program, Geneva, Switzerland, 2007.
- Wu, W.-S., Purser, R. J., and Parish, D. F.: Three-dimensional variational analyses with spatially inhomogeneous covariances, *Mon. Weather Rev.*, 130, 2905–2916, 2002.

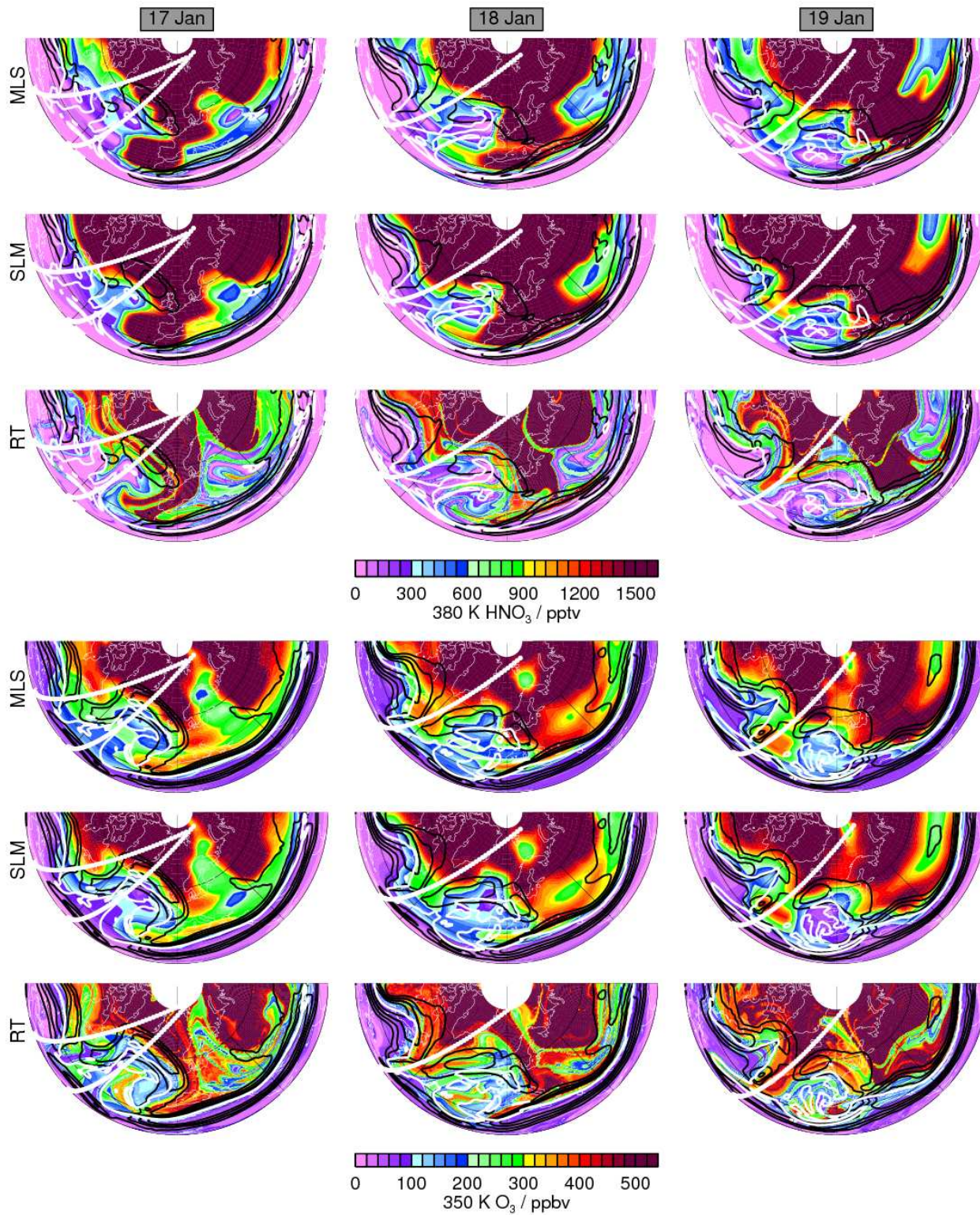


Fig. 10. Maps of (top to bottom for each level/species) MLS, SLIMCAT and RT (see text) 380 K HNO_3 (top set) and 350 K O_3 (bottom set) near the beginning of the 2006 SSW. White contour shows the 4.5 "PV Unit" contour that is commonly used as an approximate definition of the extratropical tropopause; black contours show windspeeds of 30, 40, 50 and 60 ms^{-1} . 0 to 90°N and -90 to 90°E is shown, with 0° longitude at the bottom. The white tracks (closely spaced white dots) show the MLS orbit tracks, with a dot at each measurement location, examined in Figure 11.

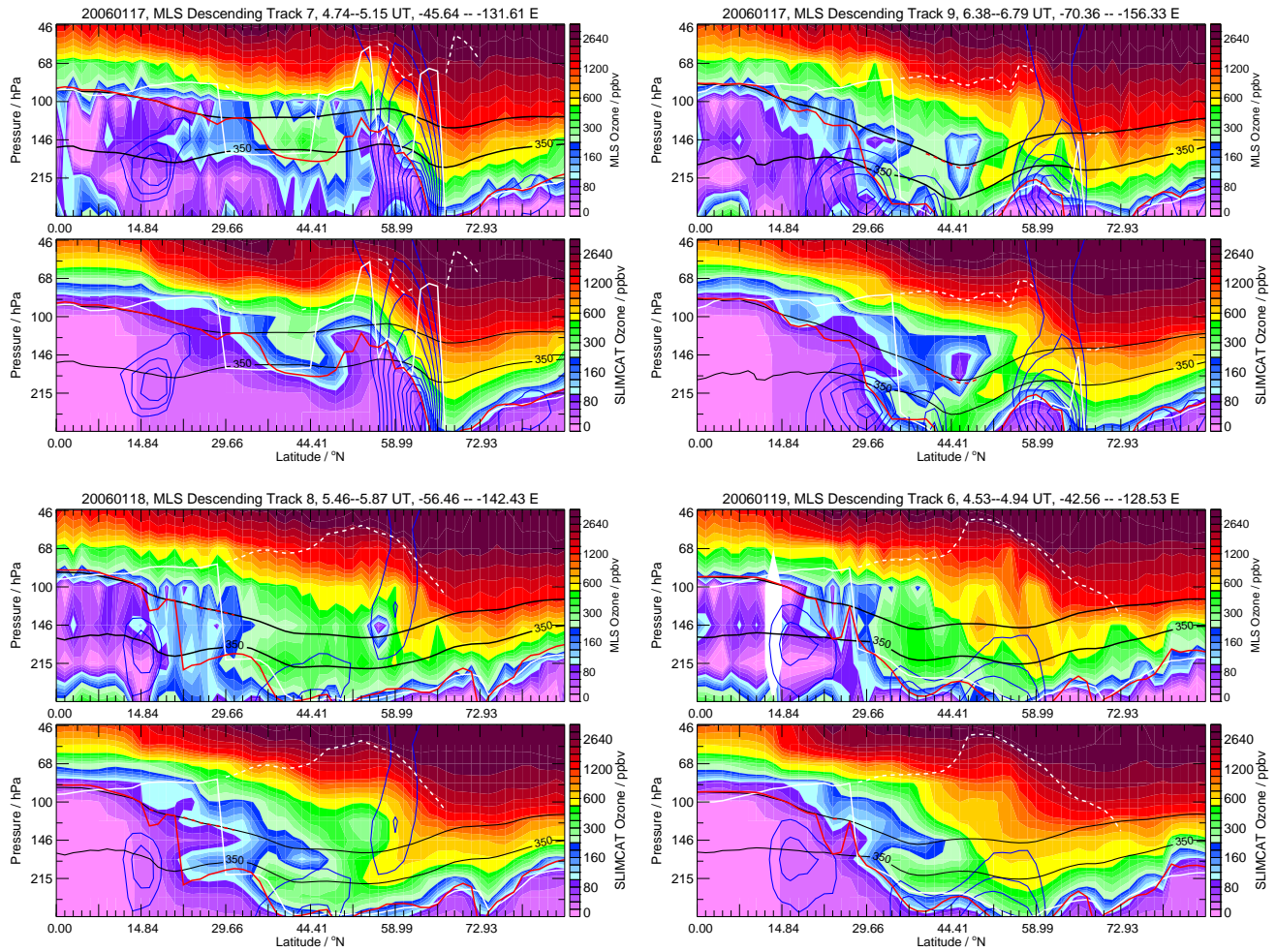


Fig. 11. Plots of MLS and SLIMCAT (top and bottom of each pair, respectively) O_3 profiles along orbit tracks on 17–19 January 2006; the orbit tracks shown are overlaid on Figure 10, with the sections at the top left corresponding to the easternmost track (nearest the Greenwich meridian) on 17 January. The white line is the thermal (WMO) tropopause from GEOS-5, and the red line the 4.5 PVU dynamical tropopause; dashed lines show secondary tropopauses where they exist. Blue contours are windspeeds from 20 to 60 m s^{-1} by 10 m s^{-1} . Black contours show the 350 and 380 K isentropes.

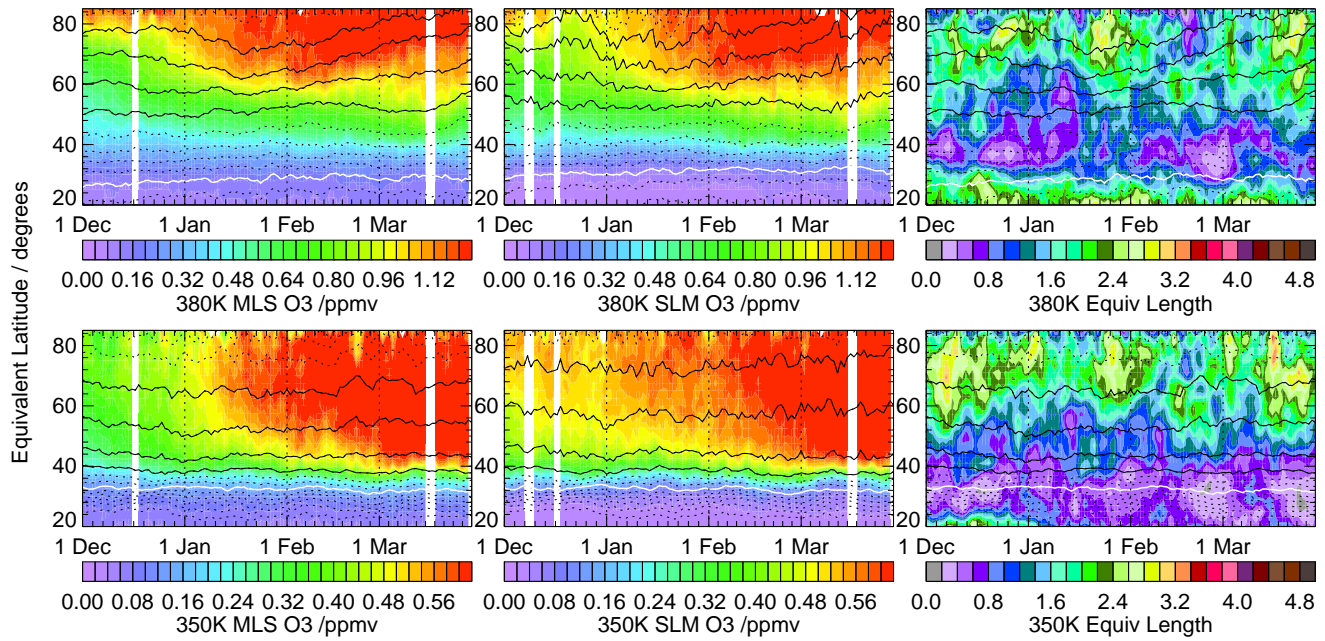


Fig. 12. As in Figure 2 but for MLS and SLIMCAT O₃ at 380 K (top) and 350 K (bottom). White overlay is the 4.5 PVU contour.

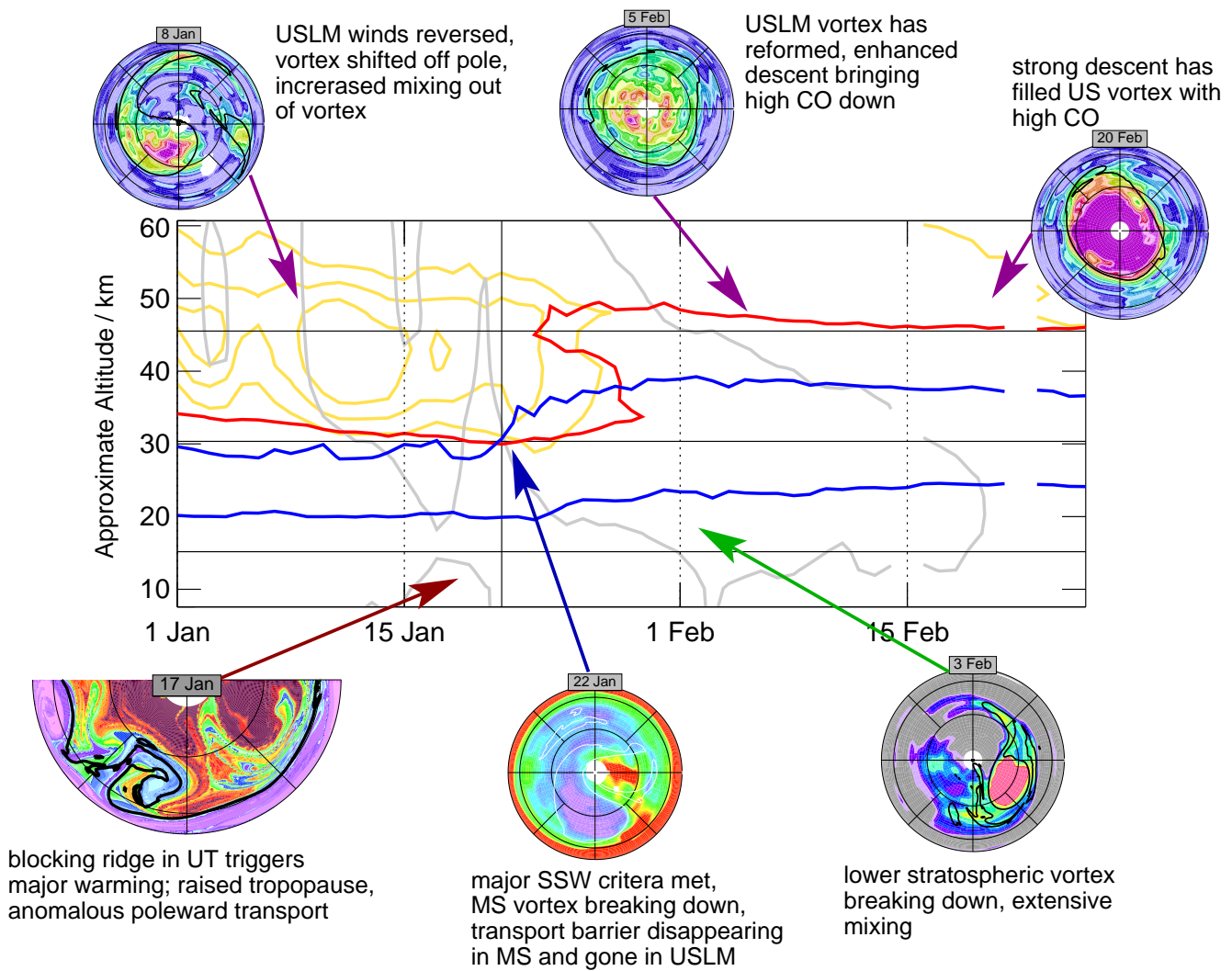


Fig. 13. Schematic of 2006 SSW and corresponding transport. Yellow lines show temperature contours in the stratopause region, grey lines the zonal mean wind zero contour. Upper stratospheric transport is illustrated by red vortex-averaged CO contour and 2500 K MLS CO maps on 8 January, 5 February and 20 February. Middle and lower stratospheric transport is illustrated by blue N_2O contours, an 850 K MLS N_2O map on 22 January, and a 520 K MLS H_2O map on 3 February. UTLS transport is illustrated by a 380 K RT O_3 map on 17 January.